

Permeability of illite-bearing shale:

1. Anisotropy and effects of clay content and loading

Ohmyoung Kwon,¹ Andreas K. Kronenberg, Anthony F. Gangi, Brann Johnson, and Bruce E. Herbert

Department of Geology and Geophysics, Texas A&M University, College Station, Texas, USA

Received 27 February 2004; revised 29 June 2004; accepted 26 July 2004; published 14 October 2004.

[1] Permeability of illite-rich shale recovered from the Wilcox formation and saturated with 1 M NaCl solution varies from 3×10^{-22} to 3×10^{-19} m², depending on flow direction relative to bedding, clay content (40–65%), and effective pressure P_e (2–12 MPa). Permeability k is anisotropic at low P_e ; measured k values for flow parallel to bedding at $P_e = 3$ MPa exceed those for flow perpendicular to bedding by a factor of 10, both for low clay content (LC) and high clay content (HC) samples. With increasing P_e , k becomes increasingly isotropic, showing little directional dependence at 10–12 MPa. Permeability depends on clay content; k measured for LC samples exceed those of HC samples by a factor of 5. Permeability decreases irreversibly with the application of P_e , following a cubic law of the form $k = k_0 [1 - (P_e/P_1)^m]^3$, where k_0 varies over 3 orders of magnitude, depending on orientation and clay content, m is dependent only on orientation (equal to 0.166 for bedding-parallel flow and 0.52 for flow across bedding), and P_1 (18–27 MPa) appears to be similar for all orientations and clay contents. Anisotropy and reductions in permeability with P_e are attributed to the presence of crack-like voids parallel to bedding and their closure upon loading, respectively. **INDEX TERMS:** 5114 Physical Properties of Rocks: Permeability and porosity; 5139 Physical Properties of Rocks: Transport properties; 5112 Physical Properties of Rocks: Microstructure; 1832 Hydrology: Groundwater transport; **KEYWORDS:** permeability, shale, connected pore space

Citation: Kwon, O., A. K. Kronenberg, A. F. Gangi, B. Johnson, and B. E. Herbert (2004), Permeability of illite-bearing shale: 1. Anisotropy and effects of clay content and loading, *J. Geophys. Res.*, 109, B10205, doi:10.1029/2004JB003052.

1. Introduction

[2] Permeabilities of shales and mudstones are much lower than those of sandstones. As a result, subsurface fluid flow may be very rapid within sandstones, while flow through shales may be so slow that departures in pore pressure from the hydrostat may be supported over geologically significant time intervals [Dickinson, 1953; Dickey *et al.*, 1968; Chapman, 1972, 1994a, 1994b; Bruce, 1973, 1984; Schmidt, 1973; Bishop, 1979; Plumley, 1980; Harrison and Summa, 1991; Bigelow, 1994]. Laboratory measurements of permeability k for intact shales, mudstones, and clay aggregates vary widely, from 10^{-16} m² to 10^{-23} m² [e.g., Young *et al.*, 1964; Bryant *et al.*, 1975; Lin, 1978; Magara, 1978; Silva *et al.*, 1981; Bredehoeft *et al.*, 1983; Tavenas *et al.*, 1983; Morrow *et al.*, 1984; Bennett *et al.*, 1989; Katsube *et al.*, 1991; Neuzil, 1994; Vasseur *et al.*, 1995; Dewhurst *et al.*, 1996a, 1996b, 1998, 1999; Schlomer and Krooss, 1997; Kwon *et al.*,

2001; Harrington *et al.*, 2001]. At the high end of this range, shale units offer little resistance to subsurface flow over long time intervals, but they may serve to divide hydrocarbon reservoirs into fluid compartments over short time intervals. At the low end of the measured range ($k \leq 10^{-22}$ m²), shales may form pressure seals to aqueous fluids, impeding fluid transport over extended, geologic times, even in the absence of capillary effects associated with nonwetting hydrocarbons [e.g., Bredehoeft and Hanshaw, 1968; Bradley, 1975; Hunt, 1990; Deming, 1994].

[3] Much of the observed variation in permeability of shales can be attributed to variations in porosity [Silva *et al.*, 1981; Tavenas *et al.*, 1983; Morin and Silva, 1984; Bennett *et al.*, 1989; Katsube *et al.*, 1991; Schlomer and Krooss, 1997; Dewhurst *et al.*, 1998, 1999], grain size and pore size distributions [Morrow *et al.*, 1984; Bennett *et al.*, 1989; Katsube *et al.*, 1991; Schlomer and Krooss, 1997; Dewhurst *et al.*, 1998, 1999], and the hydrostatic pressures (or unidirectional loads) applied during testing [Young *et al.*, 1964; Magara, 1978; Neglia, 1979; Lin, 1978; Morrow *et al.*, 1984; Katsube *et al.*, 1991; Vasseur *et al.*, 1995; Dewhurst *et al.*, 1998, 1999; Kwon *et al.*, 2001]. However, shales also exhibit wide ranges in fabric and clay content. Anisotropy in transport properties may

¹Now at Core Laboratories, Petroleum Services, Houston, Texas, USA.

be pronounced in clay-bearing sediments and soils which exhibit grain shape alignments [Al-Tabbaa and Wood, 1987; Bennett et al., 1989; Leroueil et al., 1992; Little et al., 1992; Vasseur et al., 1995; Bolton et al., 2000], but only a few studies have examined permeability anisotropy for well consolidated (or fissile) shales [Young et al., 1964; Lin, 1978]. Permeabilities of clay-bearing aggregates have also been found to depend, at a given porosity, on clay mineral content [Silva et al., 1981; Tavenas et al., 1983; Dewhurst et al., 1998, 1999; Revil and Cathles, 1999].

[4] In an earlier study of fluid transport along bedding of Wilcox shale, we found that bedding-parallel permeabilities were lower in stratigraphic horizons of higher clay content [Kwon et al., 2001]. We also found that reductions in bedding-parallel k with increasing effective pressure P_e could be described by a cubic law of the form

$$k = k_0[1 - (P_e/P_1)^m]^3, \quad (1)$$

where k_0 , a reference permeability at $P_e = 0$, is sensitive to clay content, effective pressure P_e is given by the simple difference between externally applied confining pressure P_c and pore pressure P_p , and parameters m and P_1 are associated, respectively, with geometry and effective stiffness of the conductive pore space [Gangi, 1978]. Given that permeability is anisotropic, we expect that the parameters k_0 , m , and P_1 vary with flow direction according to the orientations, dimensions and properties of fluid conduits. In addition, the values of k_0 , m , and P_1 we determined for permeability upon loading are not likely to describe fluid transport upon unloading. With increasing effective pressure, pores of weak solids may close irreversibly and several studies of shale (and clay aggregate) permeabilities have revealed effects of load cycling [Olsen, 1972; Lin, 1978; Morrow et al., 1984; Dewhurst et al., 1998], consistent with stress-volume relations of soils [Schofield and Wroth, 1968; Scott, 1980; Wood, 1990; Olgaard et al., 1995].

[5] Transport properties of shales and mud rocks ultimately depend on the interconnected pore space. Much has been learned about pore size distributions from measured capillary pressures and specific surface areas [Silva et al., 1981; Tavenas et al., 1983; Katsube et al., 1991; Schlomer and Krooss, 1997; Dewhurst et al., 1998, 1999]. However, sensitivities of permeability to flow direction, clay content, and loading cannot be understood fully without further information regarding relationships between clay microfabrics and the sizes and shapes of pores, and the mechanical response of clays (elastic and inelastic) surrounding pores. Advances in understanding the transport properties of sandstones have come from the microstructural characterization of pore space [e.g., Bernabé, 1991; Fredrich et al., 1993] and network modeling based on systems of characteristic conduits [e.g., Gangi, 1978; David, 1993; Zhu et al., 1995]. Pore fabrics of clay-bearing sediments differ significantly from those of sandstones [Lee et al., 1985; Kim et al., 1998, 1999; Hildenbrand and Urai, 2003]; yet only few studies of transport properties have been accompanied by microstructural observations of pores in shales and mudstones [Bennett et al., 1989; Katsube and Williamson, 1994; Vasseur et al., 1995].

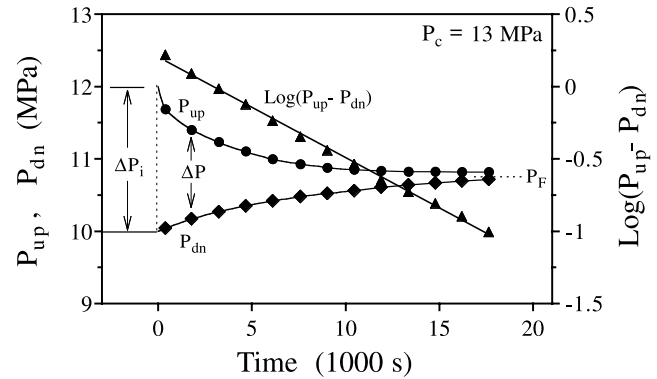


Figure 1. Raw fluid pressure in upstream reservoir P_{up} , fluid pressure in downstream reservoir P_{dn} and $\log(P_{up} - P_{dn})$ versus time data used to determine permeability by transient pulse method (experiment WS2.7-1). Initially, fluid pressure in the upstream reservoir P_{up} and fluid pressure in the downstream reservoir P_{dn} were equal (their common value, P_f was taken to equal P_p within samples once P_f showed no variation with time). After applying the initial pressure difference ΔP_i (at $t = 0$) across the sample length, P_{up} declines with time and P_{dn} increases, both approaching a new equilibrium fluid pressure P_f . Recast as $\log(P_{up} - P_{dn})$ versus time t , these data follow a line with a slope of $-\theta/2.303$ (equation (2)), which can be used to determine permeability k by equation (3).

[6] In this paper, we report on an experimental study of permeability of a low-porosity, illite-rich shale from the Wilcox formation designed to examine anisotropy relative to bedding, the influence of clay content, and effects of loading on fluid transport. Accompanying these measurements, we use electron microscopy to examine relationships between clay mineral fabrics and intergranular pores and make interpretations of permeability anisotropy and observed changes in k upon cyclic loading. All results reported here apply to the flow of 1 M NaCl solution; effects of fluid composition on permeability of Wilcox shale are addressed in a companion study [Kwon et al., 2004].

2. Experimental Methods

2.1. Permeability Measurements

[7] Permeabilities were determined by a transient pulse method [Brace et al., 1968; Sutherland and Cave, 1980; Trimmer, 1981]. For each permeability determination, we imposed a step in fluid pressure at one end of a cylindrical specimen (25.4 mm long and 12.5 mm in diameter) and measured the time variation in the fluid pressure difference across its length. Once the desired P_c and P_p values of the test were achieved, the upstream fluid pressure reservoir in contact with one specimen end was isolated from the downstream reservoir in contact with the opposite specimen end. The pressure in the upstream reservoir was then increased by an amount ΔP_i ($\leq 15\%$ of the initial P_p) using a HIP (High Pressure Equipment Co.) pressure generator (Figure 1). Following the application of a fluid pressure difference across the sample, the pressure of the upstream fluid reservoir P_{up} was observed to decay, and the pressure of the downstream reservoir P_{dn} was observed to increase,

both approaching a final equilibrium fluid pressure P_F by flow through the specimen. Both P_{up} and P_{dn} were measured to ± 0.02 MPa using high-sensitivity Dynisco PT130 transducers (with resolution limited by an output measurement error of ± 0.01 mV).

[8] The time variation of either P_{up} or P_{dn} can be used to determine the axial permeability of the specimen [e.g., *Brace et al.*, 1968; *Kwon et al.*, 2001]. However, daily fluctuations in ambient temperature ($\pm 1-2^\circ\text{C}$) of the fluid reservoirs led to fluctuations in fluid pressure (± 0.08 MPa) greater than instrumental resolution, and the time variation of the pressure difference $\Delta P = (P_{up} - P_{dn})$ proved to be much less sensitive to temperature. Temperature fluctuations of the pore pressure system were minimized by wrapping insulation around the fluid reservoirs and plumbing. Temperatures of the upstream and downstream reservoirs at all times were indistinguishable.

[9] To make sure that the observed reductions in pressure gradient across samples corresponded to flow through the sample, rather than to flow between the sample and jacket, fluid pressure stepping experiments were performed on an aluminum sample using the same jacket arrangement and methods used in the permeability experiments. These tests showed that flow between the sample and jacket is negligible at confining pressures P_c that exceed the fluid pressure P_f by ≥ 0.5 MPa. All permeabilities of specimens were measured at $(P_c - P_f) \geq 2$ MPa.

[10] Fluid pressures in the upstream and downstream reservoirs were monitored until the difference between the two ($P_{up} - P_{dn}$) dropped by at least half of the initial pressure difference (ΔP_i) imposed at $t = 0$, and the data were fit by

$$(P_{up} - P_{dn}) = \Delta P_i e^{-\theta t} \quad (2)$$

to find θ . Assuming that terms describing fluid storage within samples can be neglected [*Brace et al.*, 1968; *Sutherland and Cave*, 1980], the value of θ (determined from the slope $\log(P_{up} - P_{dn})$ versus t in Figure 1 and multiplying by -2.303) can be expressed

$$\theta = (kA/\eta\beta L)(1/V_{up} + 1/V_{dn}), \quad (3)$$

where k is permeability, A and L are the cross-sectional area and length of the sample, respectively, η is the absolute (dynamic) viscosity of the fluid, β is the compressibility of the fluid, and V_{up} and V_{dn} are upstream and downstream reservoir volumes, respectively. The viscosity η of the NaCl solution at $\sim 20^\circ\text{C}$ was taken to be 1.1×10^{-9} MPa s [*Wolf et al.*, 1979] and its compressibility was assumed to be similar to that (4.56×10^{-4} MPa $^{-1}$) of water [*Meyer et al.*, 1979]. Volumes of upstream (15.1 mL) and downstream (24.4 mL) reservoirs of the fluid pressure system were determined from their effective compressibilities after purging the system of air, isolating each reservoir, and imposing steps in pressure much like those in the permeability experiments. On the basis of these volumes and determinations of connected porosity for our samples, the ratio of sample pore volume to the upstream reservoir volume was 0.02 and that of the pore volume relative to the downstream reservoir was 0.013. Errors in permeability

associated with fluid storage terms for these volume ratios are less than $\sim 1\%$ [*Trimmer*, 1981].

[11] The scatter in measured permeabilities is dominated by real sample-to-sample variations. Observed variations in both fluid pressure measurements P_{up} , P_{dn} for individual transient pulse experiments correspond to ambient temperature fluctuations, but variations in the pressure difference ($P_{up} - P_{dn}$) are essentially equal (± 0.02 MPa) to instrumental error. On the basis of least squares fitting of $\log(P_{up} - P_{dn})$ versus time data [*York*, 1966], permeability k can be determined from slope θ with a standard deviation of 1–3%, neglecting any errors in absolute reservoir volumes or values of fluid viscosity and compressibility. However, based on the scatter of sequential permeability measurements with increasing P_e for individual samples about any chosen, smoothly varying function of k and P_e , uncertainties in permeability appear to be closer to $\pm 10\%$. These variations probably reflect real variability in pore closure as P_e is increased. Samples that were unloaded from elevated effective pressure P_e to 3 MPa and reloaded to the same or higher P_e show systematic reductions in k that fall within the observed $\pm 10\%$; however, determinations of k following unloading (and reloading) are of lower quality than measurements for samples that were not subjected to this procedure. Despite our efforts to change effective pressure systematically during load cycling, additional non-recoverable changes in porosity may have occurred during this procedure.

[12] Specimens for permeability measurements were selected to fall into two categories, one with similar high clay contents HC (65%) and the other with similar low clay contents LC (40%). Uncertainties in absolute clay content, porosity and microstructure are difficult to evaluate. Yet, sample-to-sample variations in these parameters for specimens of a given clay content (but taken from different stratigraphic horizons) result in permeability variations (of $\pm 70\%$) that greatly exceed instrumental measurement error.

[13] Confining pressures P_c during transient pulse measurements of k were controlled to within ± 0.2 MPa and measured to within ± 0.06 MPa, leading to an uncertainty in the reported, mean value of $P_e = (P_c - P_p)$ of ± 0.07 MPa just before the upstream fluid pressure P_{up} was increased to impose a fluid pressure gradient. Once P_{up} was increased, true $P_e = (P_c - P_p)$ values varied within the specimen, both spatially and temporally. Immediately after increasing P_{up} , the effective pressure P_e at the upstream sample end was reduced by as much as 30%, while P_e at the opposite end was unchanged. During the course of each transient pulse experiment, ($P_c - P_p$) in upstream portions of the sample increased with time as ($P_c - P_p$) in downstream portions decreased, both approaching a final, equilibrium value somewhat smaller than the initial P_e .

[14] Given that permeability of Wilcox shale is lower at higher effective pressure, we expect that bulk permeabilities determined for samples with axial gradients in P_e are dominated by locally lower permeabilities where P_e is higher. In addition, because shale permeabilities do not change much upon unloading, in comparison to changes observed upon initial loading [*Lin*, 1978; *Dewhurst et al.*, 1998], we do not expect that k increased much at the reduced values of P_e . On the basis of these considerations, we made no corrections to values of P_p or P_e and

simply report their values determined before P_{up} was increased.

[15] Permeabilities k were compared at fixed values of effective pressure P_e for flow parallel and perpendicular to bedding of high and low clay content specimens subjected to systematically increasing P_e and, for some specimens, following decreases in P_e as well. We also examined effects of flow direction, clay content and loading history by best fitting paired k , P_e values to the cubic law (1) in log $[1 - (k/k_0)^{1/3}] - \log P_e$ space and comparing parameters k_0 , m and P_1 . Values of parameters m and P_1 were determined by linear regression methods, where m is given by the slope in log $[1 - (k/k_0)^{1/3}] - \log P_e$ and P_1 is given by the intercept ($-m \log P_1$), and regression was repeated, iterating on k_0 to minimize error.

2.2. Shale Characterization

[16] Specimens used in this study were prepared from shale core of the Wilcox formation recovered from depths of ~ 3955 m (12,975 feet) to 3959 (12,989 feet) in West Baton Rouge Parish, Louisiana (generously provided by R. R. Berg). An in situ pore pressure of 63 MPa (9100 psi) was estimated for this interval on the basis of mud weight; this value exceeds normal hydrostatic values observed elsewhere in the Gulf Coast [Dickinson, 1953; Schmidt, 1973] and limits the pressure difference between overburden and pore pressure to ~ 26 MPa. A temperature of 121°C (250°F) was measured at the bottom of the well bore, significantly greater than the dehydration temperature ($\sim 105^\circ\text{C}$) of the smectite-illite transition [Burst, 1969; Eberl and Hower, 1976]. Porosities measured from well logs range from 2.5 to 15% (records from Reese Oil and Gas Intracoastal Land Co well 2), with higher porosities corresponding to intervals of lower clay content. Upon acquisition of the core, the shale contained 2.1 wt % water (as determined by weight loss upon heating representative material to 210°C). However, the original pore fluid content of the core was probably not preserved during earlier storage.

[17] Shale composition, clay microfabric, porosity, and textural relationships between clays and pores were characterized by optical and electron microscopy, X-ray diffraction, and weight gain upon saturation by fluid. Clay mineral contents of core used in this study were determined optically, taking point counts along traverses perpendicular to bedding and finding average values at the specimen scale. On the basis of these determinations and qualitative scanning electron microscopy observations, two suites of core were selected for permeability measurements (Figure 2), one of relatively high clay content HC (65%, core taken from depths of 3956 to 3959 m) and one of relatively low clay content LC (40%, depths of 3955 to 3956 m). Clay mineralogy was further characterized by X-ray diffraction of dry and wet powder samples and compared with previous determinations using dehydrated and glycerated samples [Ibanez and Kronenberg, 1993]. Preferred clay mineral alignments relative to bedding were previously determined by X-ray pole figure goniometry (methods described by Kocks et al. [1998]).

[18] Connected porosities at the specimen scale were determined by measuring weight gain of samples upon saturation by 1 M NaCl solution, assuming that the original material was nominally free of pore fluid, and using the

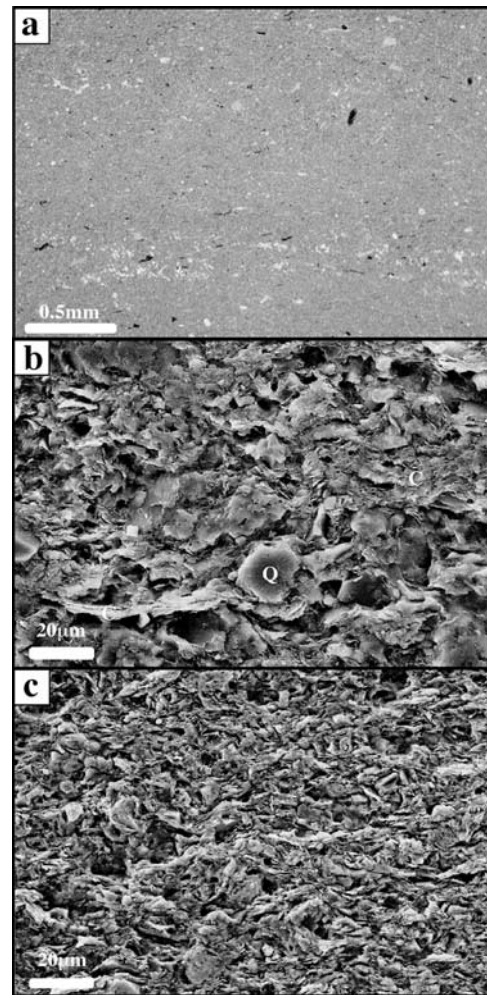


Figure 2. Scanning electron microscope images of Wilcox shale (bedding parallel to long dimension of each image). (a) Low-magnification backscattered electron micrograph illustrating the tight nature of Wilcox shale and compositional layering parallel to bedding (decorated by anhedral pyrite grains that appear light in backscattered electron images; most of the black regions in this image are due to plucking of clay packets). (b) Secondary electron micrograph of low clay content section. Clusters of subeuhedral, framboidal pyrite and detrital quartz (Q) are common, surrounded by clay platelets (C). (c) Secondary electron micrograph of high clay content section. Clay mineral grains form wavy and discontinuous sheets, stacked as layers parallel and subparallel to the macroscopically defined bedding plane.

density of 1 M NaCl solution (1040 kg/m^3) [Wolf et al., 1979]. For one set of samples, connected porosity was determined from the weight change following saturation by 1 M NaCl solution with vacuum applied, and for another set, porosity was determined following fluid saturation at pressure ($P_f = 10$ MPa). Connected porosities determined by vacuum saturation and pressure saturation procedures were comparable (within 0.2%) for samples taken from the same interval.

[19] Clay microfabrics, interstitial pore geometries, and textural relationships between clays and pores were exam-

ined in detail by scanning electron microscopy (SEM) of cut and finished specimen surfaces and transmission electron microscopy (TEM) of thin foils using methods described by *Wenk* [1976]. Specimens prepared for observational study were injected with an aliphatic epoxy resin (Eponate 12 by Pelco) prior to mechanical grinding in order to minimize damage to fine pores and microstructures. Rather than rely on pressure gradients (in vacuum or pressure injection methods) to introduce resin into the fine pores of the shale, a diffusive penetration technique was used [*Finck*, 1960; *Luft*, 1961] involving (1) dehydration, (2) infiltration, and (3) polymerization. Specimens with cut surfaces were subjected to dehydration by immersion in a gradational series of water-ethyl alcohol mixtures, starting with a 1:1 mixture, followed by mixtures that were sequentially increased in alcohol content by 10%, and finishing with 100% ethyl alcohol. Dehydrated samples were then immersed in a series of resin-propylene oxide mixtures to replace alcohol within pores by resin, starting with a 1:4 resin-propylene oxide mixture and incrementally increasing the resin content by 20% in each successive bath. Once the sample was immersed in 100% resin, it was heated in an oven at 60°C to cure the resin *in situ*.

[20] For SEM observations, cut surfaces of the resin-injected samples were ground and finished mechanically using sequentially finer Al₂O₃ grit to 3 μm, and sputter coated by gold palladium. For TEM observations, thin foils were prepared from resin-mounted thin sections, fixing 3 mm diameter nickel grids to the sections (with epoxy) and removing the nickel grid sample mounts from the glass for argon ion milling to thicknesses of <1 μm. Secondary electron and backscattered electron SEM observations were made using a JEOL JSM-6400 instrument operating at 15 kV, choosing imaging conditions to highlight textural and compositional variations. Bright-field TEM observations were made using a JEOL 2010 instrument operating at 200 kV.

2.3. Specimen Preparation, Saturation and Pressurization

[21] Prior to permeability measurements, specimens were prepared and experimental conditions applied in a uniform manner so as to obtain transport properties for comparable shale character and hydration states. Cylindrical specimens were diamond cored, and their ends were ground perpendicular to the core axis and parallel to each other to within ~0.2°. The connected pore space of each sample was saturated by 1 M NaCl solution, adding ~2.7 wt % fluid to the original water content.

[22] Samples were placed in heat shrinkable polyolefin jackets with a thin coat of RTV silicone applied to their cylindrical walls to form a seal to fluid flow between the sample and jacket. They were then immersed in a 1 M solution of NaCl over a period of >2 days, repeatedly applying a vacuum (>10 times) and bleeding atmospheric pressure back into the vacuum chamber to introduce as much fluid into pores of the sample as possible. Specimens were stored, immersed in NaCl solution until their jackets were sealed, pressurized, and their permeability measured. While exposure of Wilcox shale to an electrolyte solution should minimize clay swelling (and related changes in pore structure), specimens were observed to

expand by 0.5%. Layers of glass fiber felt (Fiberfrax, Carborundum Corp.) were placed at both ends of each sample to ensure uniform access of pore fluid to the specimen ends and pistons with pore pressure ports were placed at both ends, inserting them into the overlapping jacket. The seal between the pistons and jacket was accomplished by way of Nichrome wires, tied over a machined groove in each piston. Once the sample assembly was placed within the pressure vessel, the portion of the pore pressure system that required disassembly between experiments was placed under a vacuum for 30 minutes (to remove trapped air) and then filled with 1 M NaCl solution.

[23] Once pore fluid was introduced, a confining pressure P_c of 3 MPa was applied (2 MPa in the case of sample WS22N). The fluid in contact with both specimen ends was then pressurized to $P_f = 2$ MPa (we distinguish P_f , the pressure measured in the pore pressure system from P_p , the fluid pressure within specimen pores as P_f may not equal P_p at first, and equilibration may require significant times for low-permeability samples), holding P_c constant. Pore fluid was then bled from the system by cracking fittings repeatedly to ensure complete filling of the pore pressure system by the fluid and to achieve saturation of samples, as judged by the sensitivity of P_f to confining pressure P_c perturbations [*Green and Wang*, 1986]. Once P_f remained constant over 4–5 hours, it was considered at equilibrium with the internal pore pressure P_p of the sample.

[24] Confining and pore pressures were increased stepwise over an extended period of time to the desired experimental conditions, taking care that the difference between confining and pore fluid pressures did not exceed the ultimate value of effective pressure at which the first permeability measurement was to be made. Once P_c and P_f remained constant at 3 and 2 MPa, respectively, P_c was increased by 2 MPa followed by an increment of 2 MPa in P_f , each time allowing 2–3 hours for pore pressure equilibration and repeating this procedure until the desired fluid pressure was reached. Once P_f was equal to the experimental, target pore pressure P_p and remained constant with time, confining pressure P_c was increased in 3 MPa steps, bleeding the pore fluid system as needed to maintain P_f and allowing ~1 hour for P_p equilibration. Once the target P_c was achieved, P_c was held constant and P_f was monitored for 3–5 hours. Throughout, we assume that internal values of pore pressure P_p were equal to the measured P_f if P_f remained constant over time; in the following, we refer to P_p when this criterion for equilibrium was satisfied.

[25] Multiple measurements of permeability were made for many of the specimens. In most experiments, each subsequent permeability measurement was made following an increase in effective pressure $P_e = (P_c - P_p)$. Effective pressure was increased between sequential permeability determinations, in a slow stepwise manner, either by increasing P_c (in 3 MPa increments) while holding P_f constant, or by decreasing P_f while holding P_c constant, allowing ~1 hour between steps. In several experiments, permeabilities were also measured following reductions in P_e in order to test for sensitivity to load path and irreversible processes of pore collapse. In these experiments, samples

Table 1. Permeability of Low Clay Content Wilcox Shale, Parallel to Bedding

Sample-Measurement	P_c , MPa	P_p , MPa	P_e , MPa	Permeability k , $\times 10^{-21} \text{ m}^2$
WS22.5-1	13	10	3	267.8 (± 1.2)
WS22.5-2	15	10	5	89.9 (± 0.8)
WS22.5-3	18	10	8	29.6 (± 0.2)
WS22.7-1	13	10	3	218.3 (± 3.2)
WS22.7-2	15	10	5	101.4 (± 1.9)
WS22.7-3	18	10	8	55.9 (± 0.7)
WS22.10-1	18	10	8	16.7 (± 0.6)
WS22.10-2	19	10	9	9.22 (± 0.2)
WS22.10-3	20.5	10	10.5	3.67 (± 0.1)
WS22.10-4	22	10	12	3.22 (± 0.1)
WS22.10-5 ^a	13	10	3	9.22 (± 0.4)
WS22.11-1	13	10	3	186.2 (± 1.7)
WS22.11-2	14	10	4	113.6 (± 0.9)
WS22.11-3	15	10	5	77.6 (± 0.9)
WS22.11-4 ^a	13	10	3	98.7 (± 1.8)
WS22.11-5	15	10	5	64.2 (± 0.9)
WS22.11-6 ^a	13	10	3	82.3 (± 1.2)
WS22.11-7	15	10	5	62.1 (± 0.6)
WS22.11-8	16.5	10	6.5	24.3 (± 0.2)
WS22.11-9	18	10	8	11.4 (± 0.2)
WS22.11-10 ^a	13	10	3	15.6 (± 0.1)
WS22.12-1	22	19	3	189.8 (± 1.9)
WS22.12-2	22	18	4	129.4 (± 0.7)
WS22.12-3	22	17	5	94.6 (± 1.6)
WS22.12-4 ^a	22	19	3	110.4 (± 1.4)
WS22.12-5	22	15.5	6.5	55.8 (± 0.3)
WS22.12-6 ^a	22	19	3	81 (± 1.1)
WS22.12-7	22	14	8	27.4 (± 0.1)
WS22.12-8 ^a	22	19	3	46.8 (± 0.6)
WS22.12-9	22	13	9	11.3 (± 0.2)
WS22.12-10 ^a	22	19	3	22.4 (± 0.4)
WS22.12-11	22	11.5	10.5	5.1 (± 0.1)
WS22.12-12	22	10	12	3.64 (± 0.1)
WS22.12-13 ^a	22	19	3	15.8 (± 0.3)
WS22.25	13	10	3	288.2 (± 2.8)
WS22.40-1	35	32	3	168.6 (± 3.2)
WS22.40-2	45	42	3	150.2 (± 3.6)
WS22.40-3	45	41	4	121.7 (± 2.7)
WS22.40-4	35	31	4	93.9 (± 1.8)
WS22.40-5	35	30	5	63.7 (± 0.8)
WS22.40-6	45	40	5	57.2 (± 0.9)
WS22.40-7	45	38.5	6.5	42.1 (± 0.4)
WS22.40-8	35	28.5	6.5	31.2 (± 0.2)
WS22.40-9	35	27	8	22.4 (± 0.1)
WS22.40-10	45	37	8	23.1 (± 0.2)
WS22.40-11	45	36	9	21.4 (± 0.3)
WS22.40-12	35	26	9	15.9 (± 0.1)
WS22.40-13	35	23	12	11.7 (± 0.1)
WS22.40-14	45	33	12	12.1 (± 0.1)

^aMeasurement at reported $P_e = 3$ MPa made after sample subjected to higher P_e and returned to 3 MPa.

were loaded cyclically, increasing P_e by the same protocol as described above to values of 5 to 12 MPa and returning ($P_c - P_f$) to 3 MPa, measuring permeability before and after each P_e increase and decrease.

3. Experimental Results

3.1. Permeability Measurements

[26] Permeabilities measured parallel to bedding are listed in Tables 1 and 2 for low and high clay contents, respec-

Table 2. Permeability of High Clay Content Wilcox Shale, Parallel to Bedding

Sample-Measurement	P_c , MPa	P_p , MPa	P_e , MPa	Permeability k , $\times 10^{-21} \text{ m}^2$
WS2.7-1	13	10	3	156.3 (± 2.8)
WS2.7-2	18	10	8	2.67 (± 0.1)
WS5.9	13	7.5	5.5	9.89 (± 0.2)
WS6.1-1	15	12	3	18.7 (± 0.2)
WS6.1-2	16	12	4	14.3 (± 0.1)
WS6.1-3	17	12	5	10 (± 0.3)
WS6.1-4	20	12	8	7.33 (± 0.1)
WS6.4	13	7.5	5.5	8.56 (± 0.1)
WS6.5	17.5	14.5	3	52.7 (± 2.8)
WS6.7-1	17	14	3	49.3 (± 0.4)
WS6.7-2	17	13	4	17.6 (± 0.3)
WS6.7-3	17	12	5	8.56 (± 0.1)
WS6.7-4	17	9	8	2.33 (± 0.1)
WS6.7-5 ^a	17	14	3	9.45 (± 0.3)
WS6.7-6	17	9	8	2.0 (± 0.1)
WS6.7-7 ^a	17	14	3	7.22 (± 0.2)
WS7.2	25.5	20	5.5	4.89 (± 0.3)
WS7.6	16.5	13.5	3	29.9 (± 0.4)
WS15.1	13	7.5	5.5	55.3 (± 0.4)
WS15.2	12	9	3	30.8 (± 0.3)
WS15.3	14.5	9	5.5	12.4 (± 0.1)
WS19.3	13	7.5	5.5	16.3 (± 0.4)

^aMeasurement at reported $P_e = 3$ MPa made after sample subjected to higher P_e and returned to 3 MPa.

tively, organized by specimen number (e.g., WS 22.5) and measurement sequence (e.g., WS22.5-1, WS22.5-2, and WS22.5-3) when multiple measurements were made on an individual specimen. Permeabilities measured perpendicular to bedding are assembled in Table 3. In most sequential permeability measurements, effective pressure was systematically increased, either by increasing P_c or decreasing P_p between transient pulse experiments. However, four specimens were subjected to pressure cycling; measurements made at $P_e = 3$ MPa, following unloading from higher P_e , are identified. Uncertainties in tabulated permeabilities reflect instrumental error and uncertainty in θ determination.

[27] Raw transient pulse data exhibit wide variations in the decay of $(P_{up} - P_{dn})$ with time (Figure 3) corresponding to permeability k that depends on flow direction, effective pressure, and shale composition. Plotting log

Table 3. Permeability of Wilcox Shale Perpendicular to Bedding

Sample-Measurement	P_c , MPa	P_p , MPa	P_e , MPa	Permeability k , $\times 10^{-21} \text{ m}^2$
<i>Low Clay Content</i>				
WS22N-1	12	10	2	19.8 (± 0.3)
WS22N-2	13	10	3	16.9 (± 0.3)
WS22N-3	15	10	5	8.89 (± 0.1)
WS22N-4	18	10	8	6.78 (± 0.2)
WS22N-5	20.5	10	10.5	6.11 (± 0.1)
<i>High Clay Content</i>				
WS15N-1	17	14	3	4.37 (± 0.1)
WS15N-2	17	11.7	5.3	1.94 (± 0.1)
WS15N-3	17	9	8	0.31 (± 0.3)

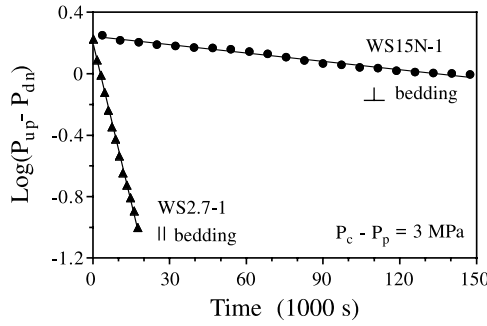


Figure 3. Raw fluid pressure data plotted as $\log(P_{up} - P_{dn})$ versus time for HC samples WS2.7 (parallel to bedding, same data as shown in Figure 1) and sample WS15N (perpendicular to bedding) at a common $P_e = (P_c - P_p) = 3$ MPa. The rapid decay of the fluid pressure gradient across sample WS2.7 relative to that of sample WS15N indicates significant anisotropy, with higher permeability (given by the steeper negative slope and equation (3)) for flow parallel to bedding and lower permeability perpendicular to bedding.

$(P_{up} - P_{dn})$ versus time, k is linearly related to the best fit slope ($= -\theta/2.303$) and calculated using equation (3). The highest permeabilities k (up to $268 \times 10^{-21} \text{ m}^2$) were measured parallel to bedding at low effective pressures for samples of relatively low clay content while the lowest values of k (down to $0.3 \times 10^{-21} \text{ m}^2$) were determined for flow perpendicular to bedding at high P_e and relatively high clay content. To isolate the dependencies of k on these variables,

we examine the data for flow parallel and perpendicular to bedding separately (Figures 4 and 5, respectively) and determine the relationship between k and effective pressure P_e for high and low clay contents. We compare the best fit relations for permeability as a function of effective pressure for different flow directions and clay content in Figure 6, and then examine effects of pressure cycling in Figures 7 and 8.

3.2. Dependence on Effective Pressure

[28] The nonlinear reduction in permeability k of Wilcox shale with increasing effective pressure P_e is well matched by the cubic $k - P_e$ relation (1) where curvature (given by parameters m and P_1), depends on flow direction, and k_0 (defined as permeability at the reference state $P_e = 0$) depends on flow direction and clay content. Permeabilities measured parallel to bedding (Figure 4a) and perpendicular to bedding (Figure 5a) show significant scatter associated with clay content and other sample-to-sample variations; yet, a drop in k of over an order of magnitude with increasing P_e is apparent, both in the accumulated data set for many samples and in the results of individual samples subjected to increasing P_e . These data, recast in terms of $\log[1 - (k/k_0)^{1/3}]$ and $\log P_e$ (Figures 4b and 5b) and best fit to relation (1), yield values of k_0 , m , and P_1 (Table 4).

[29] For a given flow direction, best fits to individual specimen results give similar values of m and P_1 to those obtained for data compiled for many specimens, but reference k_0 values vary significantly from one sample to another. As a result, the fit to the cubic law (1) is improved if we allow k_0 to vary amongst samples (as reflected in the standard deviations about the mean k_0 values for LC and HC samples, Table 4) and normalize by individually deter-

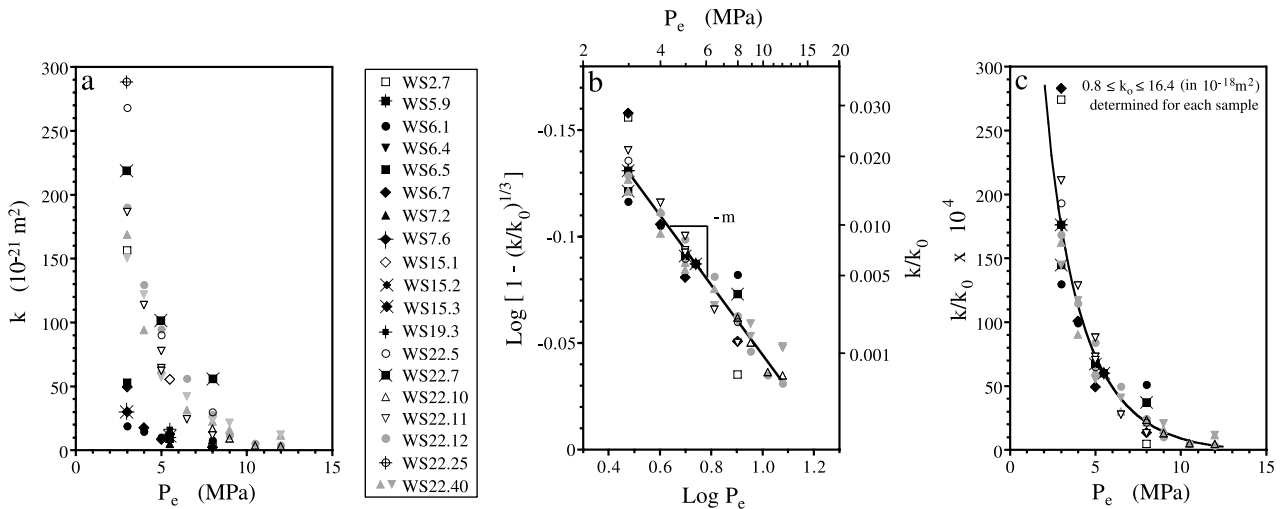


Figure 4. Permeabilities of Wilcox shale parallel to bedding, plotting entire data sets of Tables 1 and 2 for systematically increasing effective pressure. (a) Permeabilities k plotted as a function of effective pressure $P_e (=P_c - P_p)$ for both LC and HC specimens. (b) Same data recast in terms of k/k_0 and P_e according to the cubic law (equation (1)) where the slope in $\log[1 - (k/k_0)^{1/3}]$ versus $\log P_e$ yields the value of m , the intercept is equal to $-m \log P_1$, and k_0 is allowed to take on different values ($11.8 \times 10^{-18} \text{ m}^2$ and $2.9 \times 10^{-18} \text{ m}^2$, respectively) in our regressions for LC and HC specimens. The left-hand side ordinate, $\log[1 - (k/k_0)^{1/3}]$, is shown reversed, so that permeability increases upward. (c) Same permeability data compared with the cubic law fit, assuming m and P_1 are constants (0.166 and 18.4 MPa, respectively), and normalizing by reference permeabilities k_0 that were individually fit for each sample.

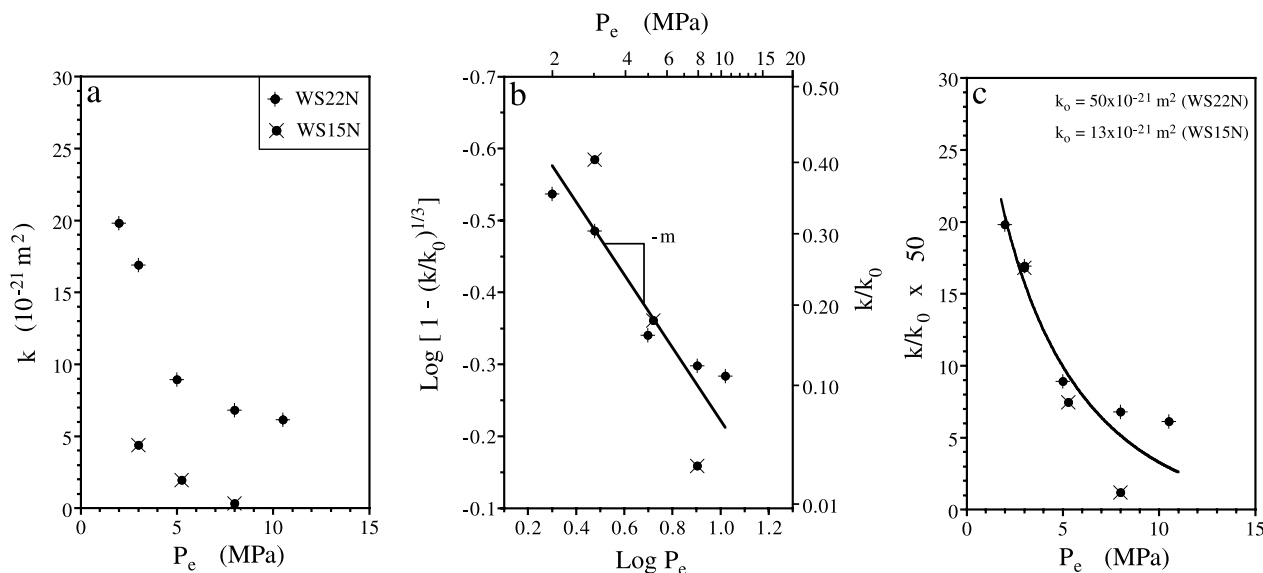


Figure 5. Permeabilities of Wilcox shale perpendicular to bedding, plotting data of Table 3. (a) Permeabilities k plotted as a function of P_e for LC and HC specimens (WS22N and WS15N, respectively). (b) Same data recast in terms of $\log [1 - (k/k_0)^{1/3}]$ and $\log P_e$ and fitted by cubic law (equation (1)) to yield values of $m = 0.52$, $P_1 = 27.0$ MPa, and $k_0 = 50 \times 10^{-21} \text{ m}^2$ and $k_0 = 13 \times 10^{-21} \text{ m}^2$, respectively, for LC and HC specimens. (c) Same permeability data compared with the cubic law fit, using a common set of m and P_1 values, and normalized by LC and HC reference permeabilities k_0 .

mined k_0 (Figures 4c and 5c). Two HC specimens (WS2.7 and WS15.1) exhibit anomalously high permeabilities parallel to bedding with best fit k_0 values ($5.7 \times 10^{-18} \text{ m}^2$ and $9.2 \times 10^{-18} \text{ m}^2$, respectively) that are closer to the mean k_0 determined for LC specimens than that for HC specimens. If the results for these two specimens are deducted from the HC data set for flow parallel to bedding, a lower mean is obtained for k_0 ($1.8 (\pm 1.0) \times 10^{-18} \text{ m}^2$) than is reported above for the entire data set.

3.3. Permeability Anisotropy

[30] Wilcox shale exhibits anisotropy in its permeability as reflected by differences in decay times for a given clay content and effective pressure (Figure 3). Permeabilities measured parallel to bedding are about 1 order of magnitude greater than those measured perpendicular to bedding at $P_e = 3$ MPa (Figures 6a and 6b) and anisotropy is predicted to be more pronounced at lower P_e . To maintain a rigorous seal between the sample and jacket, a nonzero ($P_c - P_p$) of ≥ 0.5 MPa was required during each transient pulse experiment; thus permeabilities were measured only at $P_e \geq 2$ MPa. However, our regressions yield reference permeability values k_0 that correspond to flow at zero effective pressure. For both LC and HC samples, best fit values of k_0 for flow parallel to bedding are more than 2 orders of magnitude greater than k_0 for flow perpendicular to bedding (Table 4). The degree of permeability anisotropy is reduced at higher P_e by the differing nonlinearities exhibited by $k - P_e$ relations parallel and perpendicular to bedding. At effective pressures $P_e \geq \sim 10$ MPa, permeability appears to be nearly isotropic.

3.4. Dependence on Clay Content

[31] Permeabilities both parallel and perpendicular to bedding depend on clay content (Figures 6c and 6d,

respectively) with higher k values measured for LC samples than for HC samples. Comparisons of data and best fit $k - P_e$ relations for LC (40% clay) and HC (65% clay) samples reveal differences in k of a factor of ~ 5 that are best accounted for by differences in mean k_0 (Table 4). Fits to the data for LC and HC samples require little or no variation in m and P_1 with clay content, over the range of clay content sampled.

3.5. Permeability During Loading and Unloading

[32] Permeabilities of individual specimens subjected to cyclic loading display significant hysteresis and path-dependent behavior, presumably due to permanent changes in pore structure. Permeabilities of HC specimen WS6.7 (Figure 7) decrease with sequentially increasing P_e (measurements 1–4 at P_e from 3 to 8 MPa) according to a cubic law ($k_0 = 4.4 \times 10^{-18} \text{ m}^2$, $m = 0.166$, $P_1 = 12.7$ MPa) similar to that determined for all of the HC data for bedding-parallel flow, but then depart from this relationship upon decreasing P_e . Permeabilities were measured twice at $P_e = 3$ MPa and at 8 MPa (measurements 4–7) while cycling P_e (by way of P_p changes at constant P_c). In the first cycle of increasing and decreasing P_e (between 3 and 8 MPa, measurements 1–5), the permeability change is large and mostly permanent. When P_e is again increased to 8 MPa (measurement 6) and decreased to 3 MPa (measurement 7), permeability changes appear more reproducible (with the fourth and sixth measurements yielding $k = 2.33 \times 10^{-21} \text{ m}^2$ and $2.0 \times 10^{-21} \text{ m}^2$, respectively at $P_e = 8$ MPa and the fifth and seventh measurements yielding $k = 9.45 \times 10^{-21} \text{ m}^2$ and $7.22 \times 10^{-21} \text{ m}^2$, respectively at $P_e = 3$ MPa); these recoverable changes in k at P_e less than the maximum P_e imposed on the sample presumably reflect the elastic response of connected pore space to pressure.

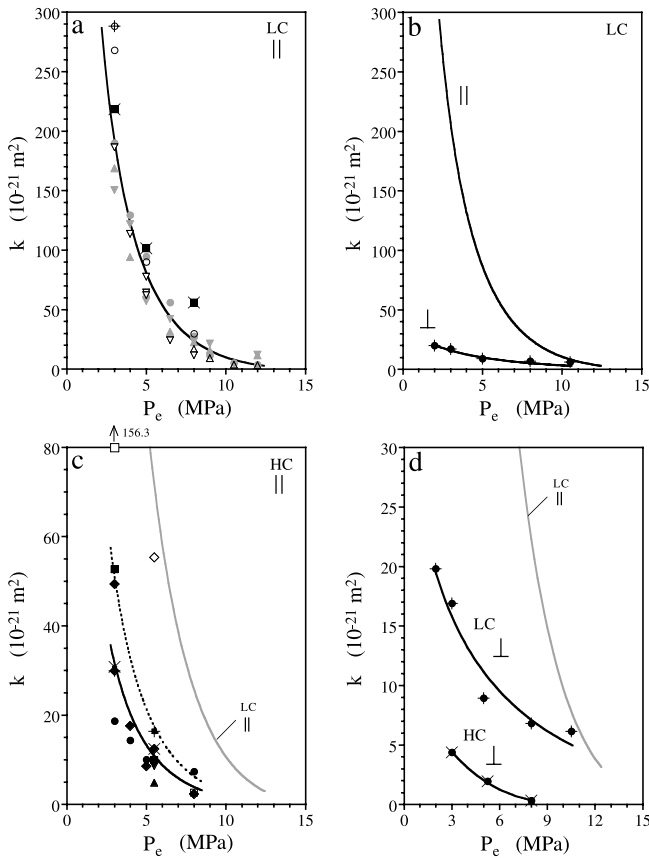


Figure 6. Permeability anisotropy and effects of clay content on fluid flow in Wilcox shale. (a) Permeabilities of low clay content (LC) samples measured parallel to bedding and fit by cubic $k - P_e$ law (same symbols as used in Figure 4). (b) Permeabilities of LC sample (WS 22N) measured perpendicular to bedding and fit by cubic $k - P_e$ law, compared with reference curve for flow parallel to bedding. (c) Bedding-parallel permeabilities of high clay content (HC) samples (same symbols as used in Figure 4), compared with reference LC curve (shown in gray). Solid black curve represents cubic $k - P_e$ law with $k_0 = 1.8 \times 10^{-18} \text{ m}^2$ (fit to data of all but two samples, WS2.7 and WS15.1), and dashed curve represents the cubic law with $k_0 = 2.9 \times 10^{-18} \text{ m}^2$ (fit to all data including outliers WS2.7-1 and WS15.1). (d) Bedding-normal permeabilities of LC and HC samples (WS22N and WS15N, respectively), fit by cubic $k - P_e$ law with common parameters m and P_1 and differing k_0 . Reference curve for bedding-parallel LC permeability is shown in gray.

Although the data are insufficient to determine a $k - P_e$ relationship for unloading, k_0 of the unloading curve must be substantially smaller than for the loading curve. Permissible values of P_1 for unloading (for m between 0.166, its loading value, and 1, its limiting value) [Gangi, 1978] are greater than P_1 for loading.

[33] Permeabilities of LC specimens WS22.10, WS22.11, and WS22.12 exhibit the same irreversible behavior as noted for HC specimen WS6.7, with similar path dependencies observed for P_c cycling (holding P_p constant, Figure 8a) as for P_p cycling (holding P_c constant, Figure 8b). Permeabilities measured at $P_e = 3 \text{ MPa}$ after unloading from a

number of points along the $k - P_e$ load curve show that decreases in k with increasing P_e are nonrecoverable as are changes in the poroelastic $k - P_e$ relationship exhibited during unloading. Slopes of $k - P_e$ unloading curves decrease as maximum applied effective pressures (the starting points for unloading) increase. Again, while parameters k_0 , m , and P_1 cannot be determined unambiguously from these data, maximum permissible values of k_0 describing fluid transport after unloading decrease and minimum permissible values of P_1 increase as samples are taken to higher maximum P_e .

3.6. Shale Composition and Fabric

[34] The bedding of Wilcox shale is expressed compositionally and texturally by (1) horizons of higher and lower clay content, (2) fine-scale laminae of higher clay content and wavy, discontinuous clay mineral packets, (3) fine-scale silty layers of higher quartz content, and (4) clay mineral alignments (Figure 2). The mineralogy inferred from X-ray diffraction of shale powder samples, measured dry, while immersed in distilled water, and immersed in 1 M NaCl, is consistent with the modal composition of 37% quartz, 29% illite, 14% chlorite, 10% kaolinite, 2% mixed illite-smectite, and 8% other solid phases (pyrite, calcite, feldspars and organics) reported by Ibanez and Kronenberg [1993]. How-

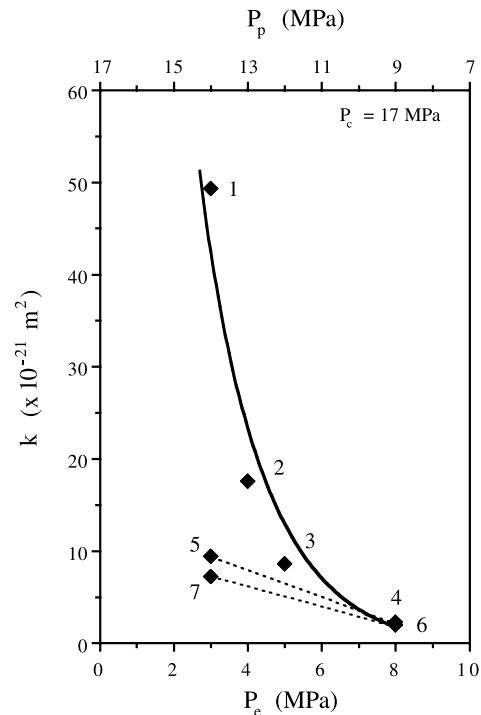


Figure 7. Changes in bedding-parallel permeability of HC Wilcox shale (WS6.7) subjected to cyclic increases and decreases in effective pressure, affected by cycling P_p (holding P_c constant) between transient pulse experiments. The sequence of permeability measurements is indicated by numbers that appear next to data. Solid curve represents fit to permeabilities measured under increasing P_e (individually fit to results of this specimen, $k_0 = 4.4 \times 10^{-18} \text{ m}^2$, $m = 0.166$, $P_1 = 12.7 \text{ MPa}$). Dashed lines represent permeability change upon decreasing P_e from 8 to 3 MPa.

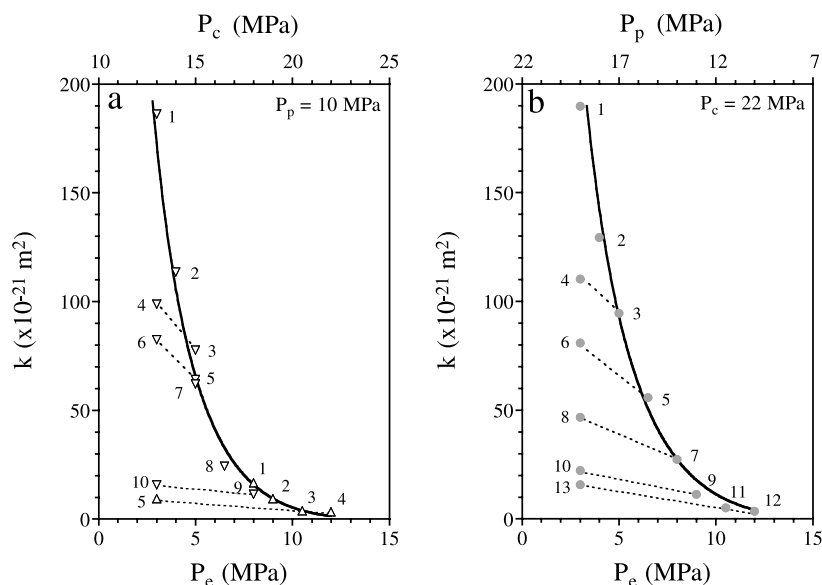


Figure 8. Bedding-parallel permeabilities of LC Wilcox shale specimens measured sequentially while loading and unloading. Numbers next to data indicate sequence of measurements, and best fit loading and unloading curves are shown as solid and dashed lines, respectively. (a) Combined results for samples WS22.10 (inverted triangles) and WS22.11 (triangles) showing large, permanent reductions in permeability upon increasing P_e (increasing P_c while holding P_p constant) and more subtle increases in permeability when P_e is returned to 3 MPa from several points along the $k - P_e$ loading curve ($k_0 = 12.0 \times 10^{-18} \text{ m}^2$, $m = 0.166$, $P_1 = 16.1 \text{ MPa}$). (b) Results for sample WS22.12 subjected to cyclic increases and decreases in P_e (by imposing decreases and increases, respectively, in P_p , holding P_c constant) showing similar permanent reductions in k with increasing P_e (fitted with $k_0 = 12.7 \times 10^{-18} \text{ m}^2$, $m = 0.166$, $P_1 = 18.4 \text{ MPa}$) and shallower, recoverable $k - P_e$ relationships that are themselves changed systematically with increasing P_e . Ascending values of P_p along the upper abscissa are shown reversed, so that P_e (lower abscissa) increases to the right.

ever optical traverses of the core show that lithology varies substantially from one horizon to the next, and that clay contents vary within a horizon at scales much smaller than the dimensions of the cylindrical cores we used for permeability tests. X-ray powder diffraction measurements reveal spatial variation in clay mineralogy with ratios of chlorite-to-illite and kaolinite-to-illite that differ by as much as 30%.

[35] Low clay content LC and high clay content HC specimens used in the permeability measurements were selected from horizons consisting of 40% and 65% mean clay content, respectively, on the basis of optical point counts and relative uniformity of the material. Clay minerals have extremely fine grain sizes (from $\sim 10 \text{ nm}$ to $10 \mu\text{m}$), as revealed by transmission and scanning electron microscopy, and they commonly occur aggregated as packets with similar lattice orientations. Quartz grains within the LC sections are homogeneously distributed compared with those in the HC sections. In HC sections, thin silty layers ($< 1 \text{ mm}$) consisting predominantly of quartz grains are intercalated with the clay-rich matrix.

[36] Clay minerals are, on average, aligned with their basal planes parallel to bedding. X-ray goniometry of illite (001) and (002) diffractions (generously provided by H.-R. Wenk) yield point maxima of poles to illite basal planes that correspond closely to the macroscopically defined bedding plane normal, with maximum densities > 4 times the expected density for randomly oriented illite grains (Figure 9a). SEM observations confirm these results (Figures 9b and 9c),

with many clay mineral platelets oriented subparallel to bedding and local variations in fabric that explain the broad nature of the (001) pole maxima. Clay minerals and clay mineral packets made of stacked face-to-face arrangements exhibit wavy basal planes throughout the material. Locally, clay platelets show larger departures from bedding, especially in the vicinity of detrital quartz (Figure 9b) and framboidal pyrite. Clay mineral packets generally show strong alignment and little pore space while domains of poorly oriented clays sometimes appear kinked or arranged in radial clusters with larger numbers of fine-scale pores.

[37] Porosities of Wilcox shale sampled in this study are low, corresponding to its depth of burial. Our microstructural observations suggest that the connected porosity is made up of a complex network of pores of differing

Table 4. Cubic Law Parameters for Wilcox Shale Permeability

	Low Clay Content	High Clay Content
<i>Flow Parallel to Bedding</i>		
k_0	$11.8 (\pm 3.4) \times 10^{-18} \text{ m}^2$	$2.9 (\pm 2.4) \times 10^{-18} \text{ m}^2$
m	$0.166 (\pm 0.008)$	
P_1	$18.4 (\pm 3.2) \text{ MPa}$	
<i>Flow Perpendicular to Bedding</i>		
k_0	$50 \times 10^{-21} \text{ m}^2$	$13 \times 10^{-21} \text{ m}^2$
m	$0.52 (\pm 0.10)$	
P_1	$27.0 (\pm 0.1) \text{ MPa}$	

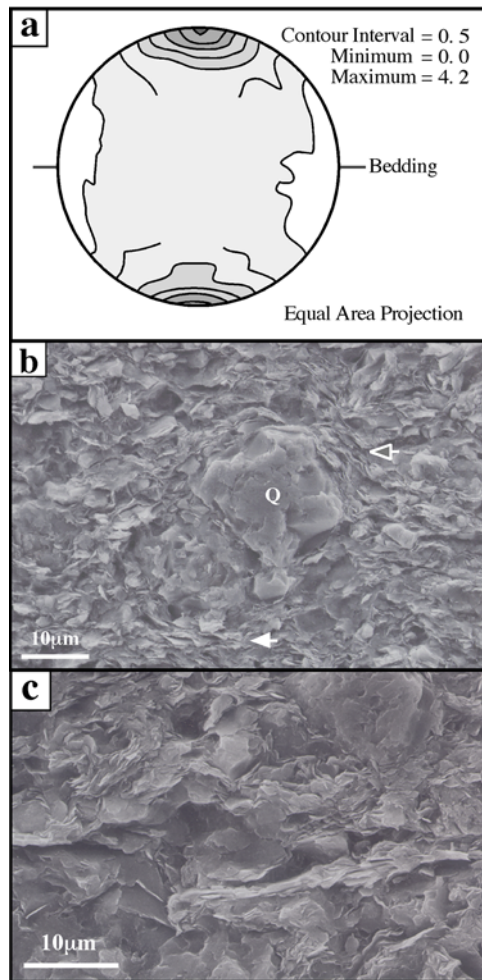


Figure 9. Clay mineral fabric of Wilcox shale relative to bedding. (a) Stereographic projection of illite (001) poles relative to bedding, measured by X-ray goniometry (thanks to H.-R. Wenk) and contoured in terms of density relative to that expected for a random distribution. (b) Secondary electron SEM micrograph of contiguous clay matrix surrounding detrital quartz grain (Q) with wavy (001) sheets subparallel to bedding (solid head arrow) and larger departures between (001) orientations and bedding (open head arrow) in the vicinity of the detrital grain. (c) Secondary electron SEM micrograph of clay matrix showing packets of similarly oriented clays in stacked face-to-face arrangements, embedded within regions of wider (001) clay mineral orientations. Bedding is parallel to the long dimensions of Figures 9b and 9c.

capacity to conduct fluid and differing resistance to closure. Weight changes upon saturation by 1 M NaCl solution yield connected porosities of 8% and 7%, respectively, for LC and HC sections. While many details of the connected pore network cannot be assessed by imaging two dimensional surfaces or thin sections, we have been able to identify and characterize at least six types of pores from SEM and TEM observations, which are prevalent throughout the material and are distinct from pores found in sandstones [Bernabé, 1991; Fredrich *et al.*, 1993].

[38] Type I pores occur as grain-scale, cleavage-parallel voids with high, crack-like aspect ratios (widths as small as

a few nm and lengths of the order of the clay grain size or less) in regions of high clay content and alignment (Figures 10a and 10b). Type II voids appear as bedding-parallel cracks within clay-rich regions that transect many clay grains (Figure 10c). These intergranular cracks typically have widths that are greater than the widths of intragranular type I voids, but they have aspect ratios that are comparable to or larger than those of type I pores. Type III pores occur at the terminations of stacked clay platelets, typically bounded by a nonbasal clay surface that terminates the mineral sheet structure and by two basal clay surfaces (Figure 11a). Type IV pores occur at face-to-edge arrangements of clay plates (Figure 11b). Type V pores are found at interfaces between clay minerals and detrital quartz and feldspar grains, as well as pyrite grains (Figure 11c).

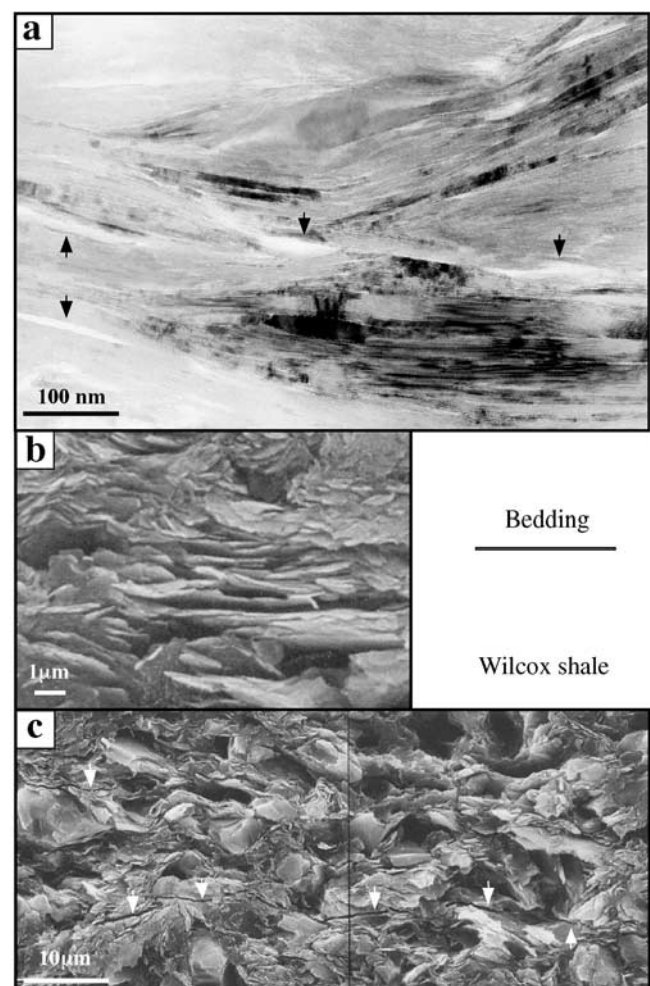


Figure 10. Pores of high aspect ratio, crack-like geometry, designated as type I and II voids. (a) TEM micrograph of fine, grain-scale type I pores (black arrows) aligned parallel to clay mineral cleavage. These pores appear parallel and subparallel to bedding in regions of high clay content that exhibit strong lattice preferred orientation. (b) SEM micrograph of type I pores within stacked, face-to-face arrangements of clay mineral grains. (c) SEM of much larger type II pores (white arrows) that consist of bedding-parallel cleavage cracks within clay rich regions and transect many clay mineral grains.

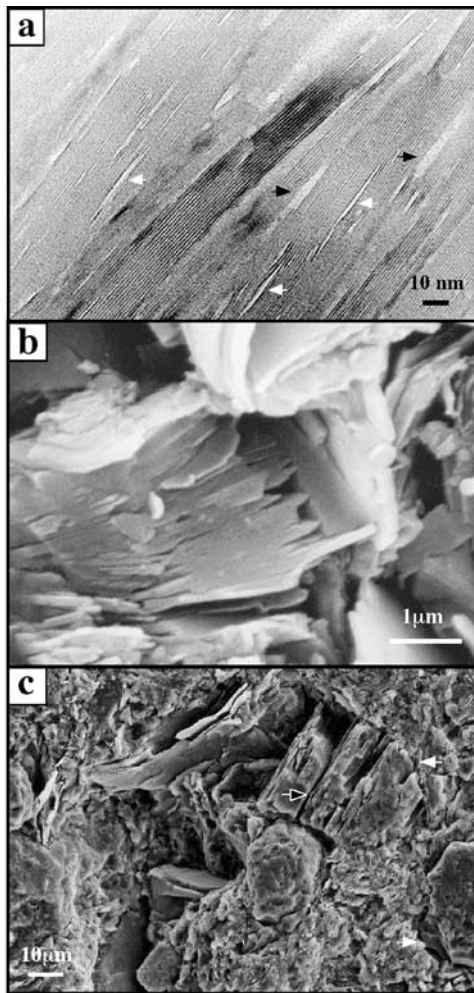


Figure 11. Geometries of type III, IV, V, and VI pores. (a) TEM micrograph of fine, wedge-shaped type III pores (shown as black arrows) that consist of voids at terminations of stacked clay platelets. Extremely fine type I pores are also indicated with white arrows. (b) SEM micrograph of type IV pores at face-edge clay mineral contacts. (c) SEM of type V pores at interfaces between clay minerals and detrital quartz, feldspar, and pyrite grains (white arrows) and type VI pores which consist of grain-scale fractures within detrital quartz and feldspar grains (black arrow).

Type VI voids appear as intragranular fractures within detrital grains (Figure 11c).

[39] Crack-like type I and II pores are present in significant numbers, and their association with aligned clays suggests that they may enhance fluid flow parallel to bedding. Type III pores have high aspect ratios as well, and they may also carry fluid parallel to local clay cleavages, in directions of the clay layer terminations. Type IV, V, and VI pores have different associations with the mineralogy of Wilcox shale, but all appear to have a wider range of orientations than type I, II, and III pores, and are likely to contribute to fluid flow in all directions relative to bedding.

4. Discussion

[40] Permeabilities measured in this study (3×10^{-22} to $3 \times 10^{-19} \text{ m}^2$) fall within the range reported for other

shales, mudstones, and clay aggregates [Young *et al.*, 1964; Bryant *et al.*, 1975; Lin, 1978; Magara, 1978; Silva *et al.*, 1981; Bredehoeft *et al.*, 1983; Tavenas *et al.*, 1983; Morrow *et al.*, 1984; Bennett *et al.*, 1989; Katsube *et al.*, 1991; Neuzil, 1994; Vasseur *et al.*, 1995; Dewhurst *et al.*, 1996a, 1996b, 1998, 1999; Schlomer and Krooss, 1997; Kwon *et al.*, 2001; Harrington *et al.*, 2001]. They compare favorably with permeabilities ($10^{-23} \text{ m}^2 < k < 10^{-20} \text{ m}^2$) measured for Eleana argillite [Lin, 1978] and shale from the Scotian shelf [Katsube *et al.*, 1991], which have clay mineralogies and porosities most similar to Wilcox shale. All measured shale permeabilities are much smaller than those of sands and sandstones (10^{-15} to 10^{-10} m^2) [Zoback and Byerlee, 1976; Walls and Nur, 1979; Bourbie and Zinszner, 1985; Brighenti, 1989; David and Darot, 1989]. As a result, shale units represent significant barriers in the subsurface to the flow of aqueous pore fluids. Thin layers of shale interbedded with reservoir (or aquifer) sand units may serve as pressure seals to cross-bedding flow over relatively short timescales [Bredehoeft and Hanshaw, 1968; Bradley, 1975; Hunt, 1990; Deming, 1994] and they may impart apparent anisotropy to composite flow properties [Bernabé, 1992]. Thick shale bodies (100–1000 m) with permeabilities comparable to our lowest measured values may form persistent seals to fluid flow over geologic times ($>10 \text{ Myr}$) [Deming, 1994].

[41] The lowest permeabilities for Wilcox shale were obtained at high effective pressure for flow perpendicular to bedding of samples with high clay contents. In the following, we assess the sensitivity of shale permeability to effective pressure, flow direction and clay content, and discuss the connected pore space responsible for transport properties.

4.1. Permeability–Effective Pressure Relation

[42] In our earlier study of bedding-parallel permeability of Wilcox shale [Kwon *et al.*, 2001], we found that reductions in k with increasing effective pressure P_e could be described by a modified cubic law (1), where P_e is given by the pressure difference ($P_c - P_p$). The fit to equation (1) of the larger data set presented here for bedding-parallel flow in low clay content specimens (yielding $k_0 = 11.8 \times 10^{-18} \text{ m}^2$, $m = 0.166$, $P_1 = 18.4 \text{ MPa}$) is comparable to our earlier determination ($k_0 \sim 10 \times 10^{-18} \text{ m}^2$, $m = 0.159$, $P_1 = 19.3 \text{ MPa}$). The cubic law also fits our data for flow perpendicular to bedding, and for samples of high and low clay content, though with differing reference permeabilities k_0 and differing sensitivities to P_e (expressed by m and P_1 , Table 4). Maximum and minimum reference permeabilities k_0 differ by 3 orders of magnitude according to flow direction and clay content. Parameter m takes on high and low values of 0.52 and 0.166 for different flow directions, and best fit P_1 values differ by $\sim 40\%$.

[43] Uncertainties in our determinations of k_0 are substantial, in part because our permeability measurements did not extend to $P_e = 0$, but more importantly because of sample-to-sample variations that probably represent real variations in lithology and pore texture. Nevertheless, differences in k_0 for flow parallel and perpendicular to bedding are large (over 2 orders of magnitude) and readily resolved. For a given flow direction, the difference in k_0 for high and low clay contents is also large; for flow parallel to bedding, the contrast in k_0 for HC and LC specimens is

probably underestimated if all data are used in the best fits. We suspect that anomalously high bedding-parallel permeabilities exhibited by two HC specimens (WS2.7 and WS15.1) are due to compositional layering and flow through thin lower clay content, higher porosity interlayers. Deleting the results of these two specimens from the analysis, the mean k_0 for HC specimens for flow parallel to bedding drops to $1.8 \times 10^{-18} \text{ m}^2$, increasing the difference between bedding-parallel k_0 values for LC and HC specimens to a factor of ~ 6 . It is difficult to assess uncertainties in k_0 from the smaller data set for flow perpendicular to bedding, but we expect that bulk permeabilities determined for this flow direction are less sensitive to compositional heterogeneity (within a given specimen) than bulk permeabilities determined for flow parallel to bedding. Cross-bedding k_0 values for LC and HC specimens differ by a factor of ~ 4 , and we expect that this difference is significant.

[44] Nonlinear reductions in k with increasing P_e for LC and HC specimens are similar for a given flow direction, and we cannot detect variations in parameters m and P_1 with clay content. However, the nonlinear response of k to P_e is markedly different for different flow directions. The uncertainty (± 0.10) in our determination of m ($=0.52$) for flow perpendicular to bedding is greater than that for flow parallel to bedding. Nevertheless, the difference between best fit m values for flow parallel and perpendicular to bedding is readily detected, with a cross-bedding m value ~ 3 times greater than the bedding-parallel m value. Best fit values of P_1 for flow parallel and perpendicular to bedding differ by $\sim 40\%$ but our confidence in distinguishing between these values is much lower, given the standard deviations about our mean P_1 values (e.g., $\pm 18\%$ for P_1 for flow parallel to bedding).

[45] The reference permeability k_0 depends on all those textural and lithologic parameters that affect the extent, geometry, and connectedness of pore space in the rock. Thus its sensitivity to flow direction relative to bedding and clay content is not surprising. Values of m and P_1 may be interpreted in terms of pore geometries and properties. Adopting the physical model upon which (1) is based [Gangi, 1978], the parameter m is related to the asperity height distribution of fluid conduits and may take on values between 0 and 1. The low value of m ($=0.166$) implies that conduits governing permeability have rough, poorly mated opposing surfaces while the higher value ($=0.52$) predicts smoother surfaces. The parameter P_1 represents an effective modulus of asperities of conduit surfaces; values of P_1 determined at increasing P_e describe the resistance to closure of pore space. Best fit P_1 values for increasing P_e are very small by comparison with static and dynamic bulk modulus κ measurements for shales ($P_1 < 10^{-2}\kappa$) [Johnston, 1987; Vernik and Nur, 1992; Johnston and Christensen, 1995; Vernik and Liu, 1997] and, as noted for other rock types [Gangi, 1978], are likely to represent inelastic response of asperities to local loads. Values of P_1 upon unloading appear to be larger than for loading, a topic we discuss later in our discussion.

[46] The cubic law applied in this study is also capable of describing the nonlinear $k - P_e$ relations reported for other shales, mudstones, and clay aggregates [Lin, 1978; Morrow et al., 1984; Katsube et al., 1991; Vasseur et al., 1995;

Dewhurst et al., 1999] with values of k_0 varying from 2×10^{-20} to $5 \times 10^{-15} \text{ m}^2$, m varying from 0.03 to 0.32, and P_1 ranging from 19 to 640 MPa. Reference permeabilities k_0 calculated for Eleana argillite data for flow parallel ($k_0 = 20 \times 10^{-21} \text{ m}^2$) and perpendicular ($k_0 = 10 \times 10^{-18} \text{ m}^2$) to the core axis [Lin, 1978], presumably perpendicular and parallel to bedding, respectively, are comparable to our values for Wilcox shale (Table 4). Reference k_0 values calculated from data for Scotian shelf shale [Katsube et al., 1991] and kaolinite aggregates [Morrow et al., 1984] are of the same order as k_0 of Wilcox shale for bedding-parallel flow. While we are confident in the values of m determined for Wilcox shale, values of m calculated for permeability data of many other argillaceous rocks and aggregates are smaller ($m \leq 0.13$). Values of P_1 calculated for permeabilities of the different shales and clay aggregates show great variation and appear to correlate with effective pressures at which permeabilities were measured. The most comparable P_1 value ($=28$ MPa for Eleana argillite) to ours is given by permeabilities measured at $3 \leq P_e \leq 24$ MPa [Lin, 1978] and the largest P_1 values ($=430$ and 450 MPa) are given by permeabilities (of kaolinite and illite aggregates, respectively) measured at $30 \leq P_e \leq 200$ MPa [Morrow et al., 1984].

4.2. Permeability Anisotropy

[47] Anisotropy in permeability of Wilcox shale is pronounced at low effective pressure; values of k at $P_e = 3$ MPa are an order of magnitude larger for flow parallel to bedding than for flow perpendicular to bedding (Figure 6), both for LC and HC specimens. Even greater anisotropy is predicted at $P_e < 3$ MPa by the cubic law and best fit k_0 values parallel and perpendicular to bedding (Table 4). Comparable permeability anisotropies have been observed for shales [Young et al., 1964; Lin, 1978], consolidated soils and clay aggregates [Al-Tabbaa and Wood, 1987; Leroueil, 1992; Little et al., 1992; Bolton et al., 2000], sheared clay and mica-bearing aggregates [Dewhurst et al., 1996a, 1996b; Zhang et al., 1999], and fault gouge [Faulkner and Rutter, 2000].

[48] The permeability of Wilcox shale becomes less anisotropic with increasing effective pressure, and measurements of k parallel and perpendicular to bedding at $P_e = \sim 10$ MPa are almost indistinguishable. This result is comparable to reductions in permeability anisotropy with pressure observed for overconsolidated marine sediments [Bolton et al., 2000]. It is in contrast to results obtained for clay aggregates undergoing shear over a range of effective stresses [Dewhurst et al., 1996a, 1996b].

[49] Models of clay aggregate compaction predict marked increases in permeability anisotropy associated with clay platelet alignment [Arch and Maltman, 1990] consistent with relationships reported between measured permeabilities and observed fabrics [Bryant et al., 1975; Leroueil et al., 1992; Little et al., 1992; Zhang et al., 1999; Faulkner and Rutter, 2000], fabrics developed during compaction [Bennett et al., 1989; Vasseur et al., 1995; Kim et al., 1999, 2001; Hildenbrand and Urai, 2003], and increases in anisotropy measured during shear [Dewhurst et al., 1996a]. Likewise, models of permeability anisotropy due to grain failure and damage within weakly cemented rocks [Bruno, 1994] predict increasing anisotropy with increasing P_e . Models of apparent anisotropy due to compositional

layering [Bernabé, 1992] do not make explicit predictions of permeability anisotropy-pressure relations. However, without large changes in permeability of one layer with respect to another, these models cannot explain the observed reductions in anisotropy with effective pressure.

[50] We do not expect that clay mineral rotations were significant in our experiments since loading was hydrostatic, initial porosity is relatively low, and clay mineral alignment is strong at the outset. Thus permeability anisotropy is not expected to change through this process. We also do not expect that grain failure was significant under the relatively modest hydrostatic loads imposed. Instead, we expect that the good fit of our permeability data to the cubic law (1) indicates that reductions in k with increasing P_e reflects the closure of cracks in the rock. Bolton *et al.* [2000] argue that the loss of permeability anisotropy in clay-bearing marine sediments is due to the closure of bedding-parallel cracks. We favor this explanation for the reduction in anisotropy observed for Wilcox shale.

[51] Differing nonlinearity in the $k - P_e$ relations for flow parallel and perpendicular to bedding is largely explained by differences in parameter m (Table 4). The relative values of m for bedding-parallel and cross-bedding flow ($m = 0.166$ and $m = 0.52$, respectively) lead to the prediction that opposing surfaces of conduits critical to bedding-parallel flow are rough and poorly mated, while those responsible for cross-bedding flow have fewer large asperities. If we fit the permeability data for Eleana argillite [Lin, 1978] to the cubic law (1), we find a similar variation in m with flow direction; assuming that Eleana argillite core was obtained with its axis perpendicular to bedding, m for flow parallel to bedding ($=0.03$) is smaller than m for flow perpendicular to bedding ($=0.32$). Similar values of P_1 for flow parallel and perpendicular to the bedding of Wilcox shale suggest that asperities of conduits that carry fluid in different directions have similar effective stiffness.

4.3. Dependence on Clay Content

[52] The effect of clay content on permeability of Wilcox shale is significant, particularly in light of the very small difference in connected porosity of high and low clay content specimens used in this study. Permeabilities of HC specimens (65% clay) are lower than those of LC specimens (40% clay) by a factor of ~ 5 , even though weight changes of specimens upon saturation suggest little variation in connected porosity (7% for HC specimens compared with 8% for LC specimens). This is consistent with results obtained for soils and marine sediments [Silva *et al.*, 1981; Tavenas *et al.*, 1983], for which permeability varies, at a given porosity, with clay content and mineralogy. An explanation for the pronounced effect of clays on permeability is offered by studies of London clay by Dewhurst *et al.* [1998, 1999], who showed that pore size distributions vary significantly with clay content, over ranges of clay content (40–67% and 27–66%) similar to that examined in this study for Wilcox shale. Thus, at comparable porosities, HC specimens may have greater numbers of fine-scale pores and smaller numbers of coarse pores than do LC specimens.

[53] Comparisons of cubic law fits to HC and LC specimen data indicate that clay content affects the value of k_0 . The common values of m and P_1 for HC and LC

specimens suggest that the geometrical character and properties of pores critical to their closure are not significantly different over the range in lithology sampled. This inference is not inconsistent with the explanation of Dewhurst *et al.* [1998, 1999] that higher clay contents are correlated with smaller numbers of coarse fluid conduits. In terms of Gangi's model for permeability [Gangi, 1978; Gangi and Carlson, 1996], the height distribution of asperities (associated with m) may be similar for large and small conduits, and the effective stiffness of asperities (related to P_1) may be comparable for large and small conduits.

4.4. Irreversible Reduction in Permeability

[54] Three lines of evidence suggest that reductions in permeability of Wilcox shale with increasing P_e are due to inelastic closure of conduits and changes in conduit asperities. These include (1) best fit values of $P_1 \ll \kappa$ determined at increasing P_e , (2) the apparent correlation of P_1 with applied P_e , as inferred by comparison of our results and others for argillaceous rocks and aggregates [Lin, 1978; Morrow *et al.*, 1984; Katsube *et al.*, 1991; Vasseur *et al.*, 1995; Dewhurst *et al.*, 1999], and (3) the irreversible reduction in k upon loading, as observed for specimens that were cyclically loaded and unloaded (Figures 7 and 8). In contrast, permeabilities measured upon unloading appear to reflect the elastic recovery of the connected pore space, unaffected by cyclic loading as long as the previous maximum P_e is not exceeded. Maximum permissible permeabilities k_0 at the reference state, $P_e = 0$, that are consistent with unloading data are $\sim 10^2$ smaller than k_0 fitted to first loading data. Minimum P_1 values consistent with the unloading data are as much as 20 times greater than P_1 values best fit to permeability data obtained at increasing P_e ; these values are still smaller than the static modulus κ , but they are comparable to the largest P_1 values calculated for any other clay aggregates [Morrow *et al.*, 1984].

[55] The large permanent reductions in k measured at increasing P_e and the smaller reversible changes in k at decreasing P_e (or during reloading at P_e less than the previous maximum P_e) mirror the behavior of uncemented soils and porous sedimentary rocks undergoing permanent porosity change during normal consolidation and recoverable elastic porosity change when the material is overconsolidated [Schofield and Wroth, 1968; Scott, 1980; Wood, 1990]. Hysteresis in measurements of specific volume, permeability, vertical strain, compressibility, and crack closure can be described by critical state models that evaluate volume-stress relations during normal consolidation, when porosity, or material state varies as stress is increased, and during unloading from a peak stress when the overconsolidated material state is fixed, set at the peak stress [Roscoe *et al.*, 1958; Fatt, 1958; Thomas and Ward, 1972; Braddock and Machette, 1976; Schoonbeek, 1976; McKown and Ladd, 1982; Brighenti, 1989; Olgaard *et al.*, 1995]. Shales of varying lithology and initial porosity exhibit specific volume-pressure relations that are described well by critical state models [Braddock and Machette, 1976; Olgaard *et al.*, 1995]; large permanent changes in specific volume and porosity define normal consolidation curves under increasing load and smaller poroelastic changes in volume upon unloading define curves of overconsolidated shale.

[56] We conclude that the large, nonrecoverable decreases observed in permeability of Wilcox shale at increasing P_e result from failure of asperities and permanent reductions in connected pore space along a consolidation curve of continuously changing state, while the small recoverable changes in k at P_e less than the previously applied maximum P_e represent the elastic response of the pore space at a constant state. On the basis of specific volume data of four shales, *Olgaard et al.* [1995] report correlations between the slopes of normal consolidation curves and porosity, and between the slopes of overconsolidated curves and the sum of porosity and swelling clay content. Similarly, differences in cubic law parameters m and P_1 for permeability of Wilcox shale and other mud rocks may reflect differences in porosity and clay mineralogy.

[57] The large, nonrecoverable changes in permeability documented for Wilcox shale suggest that variations in permeability of argillaceous units within sedimentary basins depend on burial history as well as current loading conditions. Erosion and unloading of shales will decrease effective pressure but permeability may not rebound to earlier, higher values. Likewise, dewatering of low-permeability shales during burial will increase pore pressure and thus decrease effective pressure, but permeabilities may not recover. Critical state theory indicates that permeability will be a path-dependent function of loading, compaction, and dewatering. Yet, it remains to be seen whether critical state theory accurately describes changes in consolidation over geologic times.

[58] Critical state theory appears to describe our laboratory measurements very well, but it is difficult to reconcile its predictions with our measurements and the natural, geologic loading experienced by our specimens. The specific volume of an uncemented sediment subjected to burial at geologic rates may be expected to follow a normal consolidation curve, along with all those physical properties that depend on porosity. During uplift and erosion, or recovery of core from depth, overburden pressures will decrease, and specific volume is expected to increase along an unloading-reloading curve [*Scott*, 1980; *Jones and Addis*, 1986]. During pressurization in the laboratory, such sedimentary rocks are expected to behave as overconsolidated material and follow an unloading-reloading curve until the experimentally applied P_e reaches the maximum in situ geologic mean effective stress. Once effective pressure exceeds the geologic preconsolidation pressure, the specific volume-pressure relation is expected to change to a normal consolidation curve.

[59] Detection of such a break in slope could serve as a useful method of inferring the maximum effective stress that a sediment has experienced [*Braddock and Machette*, 1976; *McKown and Ladd*, 1982; *Holbrook et al.*, 1993; *Bowers*, 1994; *Olgaard et al.*, 1995; *Ward et al.*, 1995]. Yet, our results appear to reflect normal consolidation behavior at $2 < P_e < 12$ MPa for shale that was recovered from a depth of ~ 4000 m at an estimated in situ effective pressure of ~ 26.5 MPa. The maximum effective pressure experienced by Wilcox shale in its geologic past may have even been greater before it became overpressured (at burial depths of ~ 3000 m) [*Dickinson*, 1953; *Schmidt*, 1973; *Berg and Habeck*, 1982]. Similarly, *Braddock and Machette* [1976] found that porosities of Pierre shale changed irreversibly

with pressure according to critical state theory in their laboratory tests, yet effective pressures estimated from the maximum depth of burial of their material exceeded those applied in their experiments. *Olgaard et al.* [1995] examined critical state compaction behavior for four different shales, including Pierre shale, and found that only one exhibited a break in specific volume-pressure slope that could be attributed to its previous, geological pressure history.

[60] *Olgaard et al.* [1995] suggest several time-dependent processes that may reset the state of consolidation of shales. Among these, interactions between clays and fluids during core recovery and storage may have led to relaxations of residual stresses between the time of core recovery and the time of our first permeability measurements (~ 10 years later). Similarly, time-dependent processes that alter consolidation state may be important over longer, geologic times.

4.5. Pores Responsible for Flow

[61] Textures of argillaceous rocks vary widely in intensity, according to consolidation and shear, yet several elements of the clay mineral fabric and the characteristic types of pores observed in Wilcox shale appear to be very common. Compositional layering of higher and lower clay content, wavy clay mineral packets, and clay mineral alignments parallel to bedding are ubiquitous in shales [*Lee et al.*, 1985; *Bennett et al.*, 1989; *Kim et al.*, 1998, 1999; *Hildenbrand and Urai*, 2003], marine sediments [*Kim et al.*, 2001], and compacted and sheared clays [*Vasseur et al.*, 1995; *Dewhurst et al.*, 1996a]. Aligned type I voids within individual clay grains and intergranular, bedding-parallel type II cracks have been observed in a number of shales and mud rocks [*Dewhurst et al.*, 1998; *Kim et al.*, 1999; *Hildenbrand and Urai*, 2003] and in marine sediments [*Bolton et al.*, 2000]. Type III voids at clay platelet terminations have been imaged in other deeply buried shales [*Lee et al.*, 1985] and we expect that type IV voids at face-to-edge clay interfaces are common as well. Type V voids at interfaces between clay minerals and detrital grains are revealed by studies of shale and mud rock porosity [*Kim et al.*, 1999; *Hildenbrand and Urai*, 2003] and type VI intragranular cracks in detrital grains may be expected in virtually all clastic rocks subjected to significant depositional loads [*Houseknecht*, 1987; *Lundegard*, 1992; *Dickinson and Milliken*, 1995; *Zhang et al.*, 1990; *Wong et al.*, 1997; *Menendez et al.*, 1996].

[62] Of the six types of pores characterized in this study, five are intimately associated with clays. They are readily distinguished from the large equant pores and tube-like intergranular spaces at grain triple junctions of sandstones that serve as nodes and critical linkages, respectively, in connected pore networks of reservoir rocks [*Seeburger and Nu*, 1984; *Doyen*, 1988; *Bernabé*, 1991; *Fredrich et al.*, 1993]. Thus the geometries of pores in shales, the physical properties of host material surrounding pores, and the network of connected pores depend on clay mineral distribution and alignment. From our microstructural observations of two-dimensional surfaces, we know relatively little about the connectedness of pores in Wilcox shale, or the three-dimensional network of pores. Nevertheless, the characteristic pores identified in this study provide qualitative

explanations of the sensitivity of permeability to effective pressure, flow direction, and clay content.

[63] Permeabilities of rocks are reduced at high effective pressures due to reductions in volume of pores that make up the connected network of the rock volume, particularly the closure of pores that serve as critical links in that network [David *et al.*, 1990; David, 1993; Zhu *et al.*, 1995]. Because of their high aspect ratios, type I and II voids may be efficient conduits to fluid flow at low effective pressures, but they are probably closed easily at high pressures and no longer contribute significantly to flow at high P_e . Type III and IV pores are considerably smaller than type I and II pores, but they are tube-like and we suspect that they are more resilient to applied loads; thus they may continue to serve as conduits at high effective pressures. Type V and VI pores may also show resistance to closure at pressure due to the higher stiffnesses of detrital grains and other nonclay minerals. All pores of types III to VI may continue to serve as fluid conduits at high P_e , but only across very short, grain-scale distances.

[64] The fit of the modified cubic law (1) to bedding-parallel permeability data at increasing P_e is consistent with the inference that type I and II voids are important links of the connected pore space. We expect that the nonlinear reduction in k with P_e represents the permanent changes in conduit asperities and conduit closure of these types of voids. The cubic law also fits the permeability data for flow perpendicular to bedding; yet, the $k - P_e$ relations for cross-bedding flow probably depend more directly on the closure of type IV, V, and VI voids. Increases in k upon unloading are expected to reflect the elastic recovery of pores that remain after pressurization, consisting mostly of type III–VI voids.

[65] The permeability anisotropy observed at low effective pressure may be explained in part by the strong alignment of crack-like type I and II voids that occur within clay-rich regions and in part by pore networks in low clay content lamellae. However, with the exception of a few HC specimens, which exhibited unusually high bedding-parallel permeabilities, we expect that the observed anisotropy in transport properties is largely governed by the presence of bedding-parallel type I and II voids. Aligned type I and II voids may provide efficient fluid transport along their long dimensions at low P_e , but not at high P_e . Much as observed by Bolton *et al.* [2000], closure of compliant bedding-parallel cracks may lead to reductions in permeability anisotropy at pressure. Our measurements of permeability for Wilcox shale at $P_e = \sim 10$ MPa are nearly identical for flow parallel and perpendicular to bedding. The irreversible reduction in permeability with P_e thus coincides with permanent reduction of anisotropy, as type I and II voids close irreversibly.

[66] The large differences in initial reference permeabilities k_0 parallel and perpendicular to bedding suggest substantial differences in the connected pore networks that carry fluid in different directions. Values of m for flow parallel and perpendicular to bedding are markedly different and suggest that asperity height distributions of pores that serve as conduits for flow parallel to bedding and across it are substantially different. However, values of P_1 , which represent effective stiffnesses of conduit asperities, are similar for both flow directions. This result is consistent

with the observation that most of the characteristic pores of Wilcox shale that may carry fluids parallel or perpendicular to bedding are bounded by clay minerals.

[67] All of the pores identified by electron microscopy, types I to VI, are common to both high and low clay content specimens, and more detailed statistical microstructural analyses would be needed to detect differences in their populations. Specific volume and porosimetry measurements of shales and argillaceous sediments suggest that clay content corresponds to different pore size distributions, and this may explain the dependence of permeability on clay content [Bennett *et al.*, 1989; Katsube *et al.*, 1991; Schlomer and Krooss, 1997; Dewhurst *et al.*, 1998, 1999]. Reference permeabilities k_0 of LC specimens are ~ 5 times larger than k_0 for HC specimens, and this may be due to different pore size distributions that make up the connected pore network. The common values of m and P_1 suggest little or no differences in geometrical height distributions or effective stiffnesses of conduit asperities for HC and LC specimens.

5. Conclusions

[68] Experimental measurements of permeability to flow of 1 M NaCl solution through illite-rich shale specimens of the Wilcox formation, combined with microstructural observations of clay mineral fabrics and pores lead to the following conclusions:

[69] 1. Permeability of shale depends on flow direction, clay content, effective pressure and sequence of loading, with measured values for Wilcox shale varying from 3×10^{-21} to 3×10^{-19} m².

[70] 2. Permeability k is anisotropic at low effective pressures $P_e (=P_c - P_p)$; values of k at $P_e = 3$ MPa are an order of magnitude larger for flow parallel to bedding ($k = 150\text{--}290 \times 10^{-21}$ m² for low clay content specimens) than k measured perpendicular to bedding ($k = 17 \times 10^{-21}$ m²).

[71] 3. In contrast, permeabilities measured at high P_e exhibit little directional dependence; values of k ($=3\text{--}12 \times 10^{-21}$ m²) measured parallel and perpendicular to bedding are comparable at $P_e = 10\text{--}12$ MPa.

[72] 4. Anisotropy at low P_e can be explained by preferential flow through crack-like grain-scale (type I) pores that are parallel to aligned clay mineral packets and crack-like intergranular (type II) voids that are parallel to bedding. Permeability at high P_e appears to be governed by a more isotropic network of pores (types III to VI), as high aspect ratio pores associated with aligned clays are closed.

[73] 5. Permeability for specimens (of similar connected porosity) depend on clay content; k of high clay content (HC, 65%) specimens are smaller by a factor of ~ 5 than those of low clay content (LC, 40%) specimens, both for bedding-parallel and cross-bedding flow.

[74] 6. Nonlinear reductions in permeability k with increasing effective pressure P_e can be described by a modified cubic law $k = k_0 [1 - (P_e/P_1)^m]^3$ where the reference permeability depends on flow direction ($k_0 = 12 \times 10^{-18}$ m² and 50×10^{-21} m² for flow parallel and perpendicular, respectively, to bedding of LC specimens) and clay content ($k_0 = 12 \times 10^{-18}$ m² and 3×10^{-18} m² for bedding-parallel flow through LC and HC specimens, respectively), m

depends on flow direction ($m = 0.166$ and 0.5 for flow parallel and perpendicular, respectively, to bedding), and P_1 does not vary much with flow direction or clay content (with values from 18 to 27 MPa).

[75] Irreversible reductions in k at increasing P_e and recoverable increases in k at decreasing P_e may be described by critical state formulations for soils, with inelastic closure of pores during normal consolidation due to failure of conduit asperities and elastic recovery during unloading. Values of k_0 estimated for decreasing P_e are $\sim 10^2$ smaller than k_0 best fit to first loading data, and values of P_1 for unloading are larger than first loading P_1 values by more than an order of magnitude.

[76] **Acknowledgments.** Many thanks go to Robert Berg and David Wiltchko for helpful discussions during the course of this study and to David Deming, Andre Revil, and an anonymous reviewer for their critical examination of this paper. Robert Berg also provided the Wilcox shale core, along with key information from its log data. We are indebted to Hans Rudy Wenk for providing us with the X-ray goniometry fabric analysis of Wilcox shale. High-resolution electron microscopy was performed in the Microscopy and Imaging Center at Texas A&M, and we received much help in image processing and analysis thanks to Ray Guillemette. We benefited from the technical support and experience of Jackie Magouirk. This study was supported by a grant from the U.S. Department of Energy, Office of Basic Energy Sciences, Division of Chemical Sciences, Geosciences and Biosciences (grant DE-FG05-87ER13711); their support is gratefully acknowledged.

References

- Al-Tabbaa, G., and D. M. Wood (1987), Some measurements of the permeability of kaolin, *Geotechnique*, *37*, 499–503.
- Arch, J., and A. Maltman (1990), Anisotropic permeability and tortuosity in deformed wet sediments, *J. Geophys. Res.*, *95*, 9035–9045.
- Bennett, R. H., K. M. Fischer, D. L. Lavoie, W. R. Bryant, and R. Rezac (1989), Porometry and fabric of marine clay and carbonate sediments: Determinants of permeability, *Mar. Geol.*, *89*, 127–152.
- Berg, R. R., and M. F. Habeck (1982), Abnormal pressures in the lower Vicksburg, McAllen ranch fields, South Texas, *Trans. Gulf Coast Assoc. Geol. Soc.*, *32*, 247–253.
- Bernabé, Y. (1991), Pore geometry and pressure dependence of the transport properties in sandstones, *Geophysics*, *56*, 436–446.
- Bernabé, Y. (1992), On the measurement of permeability in anisotropic rocks, in *Fault Mechanics and Transport Properties of Rocks*, edited by B. Evans and T.-F. Wong, pp. 147–167, Academic, San Diego, Calif.
- Bigelow, E. L. (1994), Global occurrences of abnormal pressures, in *Studies in Abnormal Pressures*, edited by W. H. Fertl, R. E. Chapman, and R. E. Hotz, pp. 1–17, Elsevier Sci., New York.
- Bishop, R. S. (1979), Calculated compaction states of thick abnormally pressured shales, *AAPG Bull.*, *63*, 918–933.
- Bolton, A. J., A. J. Maltman, and Q. Fisher (2000), Anisotropic permeability and bimodal pore-size distributions of fine-grained marine sediments, *Mar. Pet. Geol.*, *17*, 657–672.
- Bourbie, T., and B. Zinszner (1985), Hydraulic and acoustic properties as a function of porosity in Fontainebleau sandstone, *J. Geophys. Res.*, *90*, 11,524–11,532.
- Bowers, G. L. (1994), Pore pressure estimation from velocity data - accounting for overpressure mechanisms besides undercompaction, paper presented at 1994 IADC/SPE Drilling Conference, Soc. of Pet. Eng., New Orleans, La.
- Brace, W. F., J. B. Walsh, and W. T. Frangos (1968), Permeability of granite under high pressure, *J. Geophys. Res.*, *73*, 2225–2236.
- Braddock, W. A., and M. Machette (1976), Experimental deformation of Pierre shale, final report, 96 pp., U.S. Air Force Geophys. Lab., Hanscom Air Force Base, Mass.
- Bradley, J. S. (1975), Abnormal formation pressure, *AAPG Bull.*, *59*, 957–973.
- Bredehoeft, J. D., and B. B. Hanshaw (1968), On the maintenance of anomalous fluid pressures, I, Thick sedimentary sequences, *Geol. Soc. Am. Bull.*, *79*, 1097–1106.
- Bredehoeft, J. D., C. E. Neuzil, and P. C. D. Milly (1983), Regional flow in the Dakota aquifer: A study of the role of confining layers, *U.S. Geol. Surv. Water Supply Pap.*, *2237*, 45 pp.
- Brightenti, G. (1989), Effect of confining pressure on gas permeability of tight sandstones, in *Rock at Great Depth*, edited by V. Maury and D. Fournaintraux, pp. 187–194, A. A. Balkema, Brookfield, Vt.
- Bruce, C. H. (1973), Pressured shale and related sediment deformation - mechanism for development of regional contemporaneous faults, *Am. Assoc. Pet. Geol. Bull.*, *57*, 878–886.
- Bruce, C. H. (1984), Smectite dehydration - its relation to structural development and hydrocarbon accumulation in northern Gulf of Mexico Basin, *AAPG Bull.*, *68*, 673–683.
- Bruno, M. S. (1994), Micromechanics of stress-induced permeability anisotropy and damage in sedimentary rock, *Mech. Mater.*, *18*, 31–48.
- Bryant, W. R., W. Hottman, and P. Trabant (1975), Permeability of unconsolidated and consolidated marine sediments, Gulf of Mexico, *Mar. Geotechnol.*, *1*, 1–14.
- Burst, J. F. (1969), Diagenesis of Gulf Coast clayey sediments and its possible relation to petroleum migration, *Am. Assoc. Pet. Geol. Bull.*, *53*, 73–93.
- Chapman, R. E. (1972), Clays with abnormal interstitial fluid pressures, *Am. Assoc. Pet. Geol. Bull.*, *56*, 790–795.
- Chapman, R. E. (1994a), The geology of abnormal pore pressures, in *Studies in Abnormal Pressures*, edited by W. H. Fertl, R. E. Chapman, and R. E. Hotz, Amsterdam, pp. 19–49, Elsevier Sci., New York.
- Chapman, R. E. (1994b), Abnormal pore pressures: Essential theory, possible causes, and sliding, in *Studies in Abnormal Pressures*, edited by W. H. Fertl, R. E. Chapman, and R. E. Hotz, pp. 51–91, Elsevier Sci., New York.
- David, C. (1993), Geometry of flow paths for fluid transport in rocks, *J. Geophys. Res.*, *98*, 12,267–12,278.
- David, C., and M. Darot (1989), Permeability and conductivity of sandstones, in *Rock at Great Depth*, edited by V. Maury and D. Fournaintraux, pp. 203–209, A. A. Balkema, Brookfield, Vt.
- David, C., Y. Gueguen, and G. Pampoukis (1990), Effective medium theory and network theory applied to the transport properties of rock, *J. Geophys. Res.*, *95*, 6993–7005.
- Deming, D. (1994), Factors necessary to define a pressure seal, *AAPG Bull.*, *78*, 1005–1009.
- Dewhurst, C. N., K. M. Brown, M. B. Clennell, and G. K. Westbrook (1996a), A comparison of the fabric and permeability anisotropy of consolidated and sheared silty clay, *Eng. Geol.*, *42*, 253–267.
- Dewhurst, C. N., M. B. Clennell, K. M. Brown, and G. K. Westbrook (1996b), Fabric and hydraulic conductivity of sheared clays, *Geotechnique*, *46*, 761–768.
- Dewhurst, C. N., A. C. Aplin, J.-P. Sarda, and Y. Yang (1998), Compaction-driven evolution of porosity and permeability in natural mudstones: An experimental study, *J. Geophys. Res.*, *103*, 651–661.
- Dewhurst, C. N., A. C. Aplin, and J.-P. Sarda (1999), Influence of clay fraction on pore-scale properties and hydraulic conductivity of experimentally compacted mudstones, *J. Geophys. Res.*, *104*, 29,261–29,274.
- Dickey, P. A., C. R. Shriram, and W. R. Paine (1968), Abnormal pressures in deep wells of southwestern Louisiana, *Science*, *160*, 609–615.
- Dickinson, G. (1953), Geological aspects of abnormal reservoir pressures in Gulf Coast Louisiana, *Am. Assoc. Pet. Geol. Bull.*, *37*, 410–432.
- Dickinson, W. W., and K. L. Milliken (1995), The diagenetic role of brittle deformation in compaction and pressure solution, Etjo sandstone, Namibia, *J. Geol.*, *103*, 339–347.
- Doyen, P. M. (1988), Permeability, conductivity, and pore geometry of sandstone, *J. Geophys. Res.*, *93*, 7729–7740.
- Eberl, D., and J. Hower (1976), Kinetics of illite formation, *Geol. Soc. Am. Bull.*, *87*, 1326–1330.
- Fatt, I. (1958), Compressibility of sandstones at low to moderate pressures, *Am. Assoc. Pet. Geol. Bull.*, *42*, 1924–1957.
- Faulkner, D. R., and E. H. Rutter (2000), Comparisons of water and argon permeability in natural clay-bearing fault gouge under high pressure at 20°C, *J. Geophys. Res.*, *105*, 16,415–16,426.
- Finck, H. (1960), Epoxy resins in electron microscopy, *J. Biophys. Biochem. Cytol.*, *7*, 27–39.
- Fredrich, J. T., K. H. Greaves, and J. W. Martin (1993), Pore geometry and transport properties of Fontainebleau sandstone, *Int. J. Rock Mech. Min. Sci.*, *30*, 691–697.
- Gangi, A. F. (1978), Variation of whole and fractured porous rock permeability with confining pressure, *Int. J. Rock Mech. Min. Sci.*, *15*, 249–257.
- Gangi, A. F., and R. L. Carlson (1996), An asperity-deformation model for effective pressure, *Tectonophysics*, *256*, 241–251.
- Green, D. H., and H. F. Wang (1986), Fluid pressure response to undrained compression in saturated sedimentary rock, *Geophysics*, *51*, 948–956.
- Harrington, J. F., S. T. Horseman, and D. J. Noy (2001), Swelling and osmotic flow in a potential host rock, in *Proceedings of the 6th International Workshop on Key Issues in Waste Isolation Research (KIWAR)*,

- edited by P. Delage, pp. 169–188, Ecole Natl. des Ponts et Chaussees, Paris, 28–30 Nov.
- Harrison, W. J., and L. L. Summa (1991), Paleohydrology of the Gulf of Mexico basin, *Am. J. Sci.*, 291, 109–176.
- Hildenbrand, A., and J. L. Urai (2003), Investigation of the morphology of pore space in mudstones - first results, *Mar. Pet. Geol.*, 20, 1185–1200.
- Holbrook, P., D. Maggiori, and R. Hensley (1993), Real-time pore pressure and fracture gradient evaluation in all sedimentary lithologies, paper presented at the SPE Offshore Europe Conference, Soc. of Pet. Eng., Aberdeen, Scotland, 7–10 Sept.
- Houseknecht, D. W. (1987), Assessing the relative importance of compaction processes and cementation to reduction or porosity in sandstones, *AAPG Bull.*, 71, 633–642.
- Hunt, J. M. (1990), Generation and migration of petroleum from abnormally pressured fluid compartments, *AAPG Bull.*, 74, 1–12.
- Ibanez, W. D., and A. K. Kronenberg (1993), Experimental deformation of shale: Mechanical properties and microstructural indicators of mechanisms, *Int. J. Rock Mech. Min. Sci.*, 30, 723–734.
- Johnston, D. H. (1987), Physical properties of shale at temperature and pressure, *Geophysics*, 52, 1391–1401.
- Johnston, J. E., and N. I. Christensen (1995), Seismic anisotropy of shales, *J. Geophys. Res.*, 100, 5991–6003.
- Jones, M. E., and M. A. Addis (1986), The application of stress path and critical state analysis to sediment deformation, *J. Struct. Geol.*, 8, 575–580.
- Katsube, T. J., and M. A. Williamson (1994), Effects of diagenesis on shale nano-pore structure and implications for sealing capacity, *Clay Miner.*, 29, 451–461.
- Katsube, T. J., B. S. Mudford, and M. E. Best (1991), Petrophysical characteristics of shales from the Scotian Shelf, *Geophysics*, 56, 1681–1689.
- Kim, J.-W., W. R. Bryant, J. S. Watkins, and T. T. Tieh (1998), Mineralogical and fabric changes of shale during burial diagenesis and their effects on petrophysical properties, *Trans. Gulf Coast Assoc. Geol. Soc.*, 48, 139–150.
- Kim, J.-W., W. R. Bryant, J. S. Watkins, and T. T. Tieh (1999), Electron microscopic observations of shale diagenesis, offshore Louisiana, USA, Gulf of Mexico, *Geo Mar. Lett.*, 18, 234–240.
- Kim, J.-W., Y.-D. E. Lee, T. T. Tieh, and W. R. Bryant (2001), Effects of laboratory consolidation on petrophysical properties of fine-grained marine sediments: Electron microscopic observations, *Mar. Georesour. Geotechnol.*, 18, 347–360.
- Kocks, U. F., C. N. Tome, and H.-R. Wenk (1998), *Texture and Anisotropy: Preferred Orientations in Polycrystals and their Effect on Materials Properties*, 676 pp., Cambridge Univ. Press, New York.
- Kwon, O., A. K. Kronenberg, A. F. Gangi, and B. Johnson (2001), Permeability of Wilcox shale and its effective pressure law, *J. Geophys. Res.*, 106, 19,339–19,353.
- Kwon, O., B. E. Herbert, and A. K. Kronenberg (2004), Permeability of illite-bearing shale: 2. Influence of fluid chemistry on flow and functionally connected pores, *J. Geophys. Res.*, B10206, doi:10.1029/2004JB003055.
- Lee, J. H., J. H. Ahn, and D. Peaco (1985), Textures in layered silicates: Progressive changes through diagenesis and low temperature metamorphism, *J. Sediment. Petrol.*, 55, 532–540.
- Leroueil, S., P. Lerat, D. W. Hight, and J. J. M. Powell (1992), Hydraulic conductivity of a recent estuarine silty clay at Bothkennar, *Geotechnique*, 42, 275–288.
- Lin, W. (1978), Measuring the permeability of Eleana argillite from area 17, Nevada test site, using the transient method, *Rep. UCRL-52604*, 11 pp., Lawrence Livermore Natl. Lab., Livermore, Calif.
- Little, J. A., D. M. Wood, M. A. Paul, and A. Bouazza (1992), Some laboratory measurements of permeability of Bothkennar clay in relation to soil fabric, *Geotechnique*, 42, 355–361.
- Luft, J. H. (1961), Improvements in epoxy resin embedding methods, *J. Biophys. Biochem. Cytol.*, 9, 409–414.
- Lundegard, P. D. (1992), Sandstone porosity loss - a big picture view of the importance of compaction, *J. Sediment. Petrol.*, 62, 250–260.
- Magara, K. (1978), *Compaction and Fluid Migration*, 319 pp., Elsevier Sci., New York.
- McKown, A. F., and C. C. Ladd (1982), Effects of cementation on the compressibility of Pierre shale, in *Geotechnical Properties, Behavior, and Performance of Calcareous Soils*, edited by K. R. Demars and R. C. Chaney, *ASTM Spec. Tech. Publ.*, 777, 321–339.
- Menendez, B., W. L. Zhu, and W.-F. Wong (1996), Micromechanics of brittle faulting and cataclastic flow in Berea sandstone, *J. Struct. Geol.*, 18, 1–16.
- Meyer, C. A., R. B. McClintock, G. J. Silvestri, and R. C. Spence Jr. (1979), *ASME Steam Table, Thermodynamic and Transport Properties of Steam*, 330 pp., Am. Soc. of Mech. Eng., New York.
- Morin, R., and A. J. Silva (1984), The effects of high pressure and high temperature on some physical properties of ocean sediments, *J. Geophys. Res.*, 89, 511–526.
- Morrow, C. A., L. Q. Shi, and J. D. Byerlee (1984), Permeability of fault gouge under confining pressure and shear stress, *J. Geophys. Res.*, 89, 3193–3200.
- Neglia, S. (1979), Migration of fluids in sedimentary basins, *AAPG Bull.*, 63, 573–597.
- Neuzil, C. E. (1994), How permeable are clays and shales?, *Water Resour. Res.*, 30, 145–150.
- Olgaard, D. L., R. Nuesch, and J. Urai (1995), Consolidation of water saturated shales at great depth under drained conditions, in *Proceedings of the 8th International Congress on Rock Mechanics*, pp. 273–277, A. A. Balkema, Brookfield, Vt.
- Olsen, H. W. (1972), Liquid movement through kaolinite under hydraulic, electric, and osmotic gradients, *Am. Assoc. Pet. Geol. Bull.*, 56, 2022–2028.
- Plumley, W. J. (1980), Abnormally high fluid pressure: Survey of some basic principles, *AAPG Bull.*, 64, 414–430.
- Revil, A., and L. M. Cathles III (1999), Permeability of shaly sands, *Water Resour. Res.*, 35, 651–662.
- Roscoe, K. H., A. N. Schofield, and C. P. Wroth (1958), On the yielding of soils, *Geotechnique*, 8, 22–53.
- Schlomer, S., and B. M. Krooss (1997), Experimental characterization of the hydrocarbon sealing efficiency of cap rocks, *Mar. Pet. Geol.*, 14, 565–580.
- Schmidt, G. W. (1973), Interstitial water composition and geochemistry of deep Gulf Coast shales and sandstones, *Am. Assoc. Pet. Geol. Bull.*, 57, 321–337.
- Schofield, A. N., and P. Wroth (1968), *Critical State Soil Mechanics*, 310 pp., McGraw-Hill, New York.
- Schoonbeek, J. B. (1976), Land subsidence as a result of gas extraction in Groningen, The Netherlands, paper presented at the 2nd International Symposium on Land Subsidence, Assoc. of Hydrol. Sci., Anaheim, Calif.
- Scott, C. R. (1980), *An Introduction to Soil Mechanics and Foundations*, 406 pp., Elsevier Sci., New York.
- Seeburger, D. A., and A. Nu (1984), A pore space model for rock permeability and bulk modulus, *J. Geophys. Res.*, 89, 527–536.
- Silva, A. J., J. R. Hetherman, and D. I. Calnan (1981), Low-gradient permeability testing of fine-grained marine sediments, in *Permeability and Groundwater Contaminant Transport*, edited by T. F. Zimmie and C. O. Riggs, *ASTM Spec. Tech. Publ.*, 746, 121–136.
- Sutherland, H. J., and S. P. Cave (1980), Argon gas permeability of New Mexico rock salt under hydrostatic compression, *Int. J. Rock Mech. Min. Sci.*, 17, 281–288.
- Tavenas, F., P. Jean, P. Leblond, and S. Leroueil (1983), The permeability of natural soft clays, II Permeability characteristics, *Can. Geotech. J.*, 20, 645–660.
- Thomas, R. D., and C. C. Ward (1972), Effect of overburden pressure and water saturation on gas permeability of tight sandstone cores, *J. Pet. Technol.*, 24, 120–124.
- Trimmer, D. A. (1981), Design criteria for laboratory measurements of low permeability rocks, *Geophys. Res. Lett.*, 8, 973–975.
- Vasseur, G., I. Djeran-Maigre, D. Grunberger, G. Rousset, D. Tessier, and B. Velde (1995), Evolution of structural and physical parameters of clays during experimental compaction, *Mar. Pet. Geol.*, 12, 941–954.
- Vernik, L., and X. Liu (1997), Velocity anisotropy in shales: A petrophysical study, *Geophysics*, 62, 521–532.
- Vernik, L., and A. Nur (1992), Ultrasonic velocity and anisotropy of hydrocarbon source rocks, *Geophysics*, 57, 727–735.
- Walls, J., and A. Nur (1979), Pore pressure and confining pressure dependence of permeability in sandstone, *Transactions of the 7th Formation Evaluation Symposium*, pp. 1–8, Can. Well Logging Soc., Calgary, Alberta.
- Ward, C. D., K. Coghill, and M. D. Broussard (1995), Pore- and fracture-pressure determinations: Effective-stress approach, *J. Pet. Technol.*, 47, 123–124.
- Wenk, H.-R. (1976), *Electron Microscopy in Mineralogy*, 564 pp., Springer-Verlag, New York.
- Wolf, A. V., M. G. Brown, and P. G. Prentiss (1979), Concentrative properties of aqueous solutions: Conversion tables, in *CRC Handbook of Chemistry and Physics*, 60th ed., edited by R. C. Weast, pp. D227–D276, CRC Press, Boca Raton, Fla.
- Wong, T.-F., C. David, and W. L. Zhu (1997), The transition from brittle faulting to cataclastic flow in porous sandstones: Mechanical deformation, *J. Geophys. Res.*, 102, 3009–3025.
- Wood, D. M. (1990), *Soil Behaviour and Critical State Soil Mechanics*, 462 pp., Cambridge Univ. Press, New York.
- York, D. (1966), Least squares fitting of a straight line, *Can. J. Phys.*, 44, 1079–1086.

- Young, A., P. F. Low, and A. S. McLatchie (1964), Permeability studies of argillaceous rocks, *J. Geophys. Res.*, *69*, 4237–4245.
- Zhang, J., T.-F. Wong, and D. M. Davis (1990), Micromechanics of pressure-induced grain crushing in porous rocks, *J. Geophys. Res.*, *95*, 341–352.
- Zhang, S., T. E. Tullis, and V. J. Scruggs (1999), Permeability anisotropy and pressure dependency of permeability in experimentally sheared gouge materials, *J. Struct. Geol.*, *21*, 795–806.
- Zhu, W., C. David, and T. F. Wong (1995), Network modeling of permeability evolution during cementation and hot isostatic pressing, *J. Geophys. Res.*, *100*, 15,451–15,464.
- Zoback, M. D., and J. D. Byerlee (1976), Effect of high-pressure deformation on permeability of Ottawa sand, *AAPG Bull.*, *60*, 1531–1542.
-
- A. F. Gangi, B. E. Herbert, B. Johnson, and A. K. Kronenberg, Department of Geology and Geophysics, Texas A&M University, College Station, TX 77843, USA. (kronenberg@geo.tamu.edu)
- O. Kwon, Core Laboratories, Petroleum Services, 6316 Windfern, Houston, TX 77040, USA.